(A New Proposal to Jefferson Lab PAC35)

Search for a New Vector Boson A' Decaying to e^+e^-

J. D. Bjorken*, R. Essig (spokesperson), P. Schuster (spokesperson)
Theory Group, SLAC National Accelerator Laboratory, Menlo Park, CA 94025

M. Graham, J. Jaros, T. Maruyama, K. Moffeit, A. Odian, R. Partridge
SLAC National Accelerator Laboratory, Menlo Park, CA 94025

N. Toro (spokesperson)
Theory Group, Stanford University, Stanford, CA 94305

P. Bosted, A. Camsonne, E. Chudakov, A. Deur, J. Gomez, O. Hansen, D. W. Higinbotham, C. W. de Jager, J. J. LeRose, R. Michaels, S. Nanda, Y. Qiang, A. Saha, B. Wojtsekhowski (spokesperson and contact person)
Thomas Jefferson National Accelerator Facility, Newport News, VA 23606

R. Lindgren, N. Liyanage, V. Nelyubin, B. E. Norum, S. Riordan
University of Virginia, Charlottesville, VA 22901

P. Markowitz
Florida International University, Miami, FL 33199

A. Glamazdin
Kharkov Institute of Physics and Technology, Kharkov 310077, Ukraine

M. Khandaker, V. Punjabi
Norfolk State University, Norfolk, VA 23504

R. Gilman, G. Kumbartzki, R. Ransome
Rutgers, The State University of New Jersey, Piscataway, NJ 08854

Jin Huang, V. Sulkosky
Massachusetts Institute of Technology, Cambridge, MA 02139

D. Armstrong, T. Averett, Bo Zhao
College of William and Mary, Williamsburg, VA 23185

M. Mihovilovič, S. Širca
Jožef Stefan Institute and Dept. of Physics, University of Ljubljana, Slovenia

G. Ron
Lawrence Berkeley National Lab, Berkeley, CA 94720

The Hall A Collaboration

January 23, 2010

*to be confirmed

Abstract

An experiment is proposed to search for a new vector boson A' with weak coupling $\alpha' \gtrsim 6 \times 10^{-8}\alpha$ to electrons ($\alpha = e^2/4\pi$) in the mass range 65 MeV $< m_{A'} <$ 550 MeV. New vector bosons with such small couplings arise naturally from a small kinetic mixing of the "dark photon" A' with the photon — one of the very few ways in which new forces can couple to the Standard Model — and have received considerable attention as an explanation of various dark matter related anomalies. A' bosons are produced by radiation off an electron beam, and could appear as narrow resonances with small production cross-section in the trident e^+e^- spectrum. We propose to search for the A' by using the CEBAF electron beam at energies of $\approx$ 1–4 GeV incident on $0.5 - 10\%$ radiation length Tungsten wire mesh targets, and measure the resulting e^+e^- pairs using the High Resolution Spectrometer and PREX septum magnet in Hall A at Jefferson Lab. With a 33-day run, the proposed experiment will achieve very good sensitivity because the statistics of e^+e^- pairs will be $\sim 10,000$ times larger in the explored mass range than any previous search for the A' boson. These statistics and the excellent mass resolution of the spectrometers allow sensitivity to α'/α one to three orders of magnitude below current limits, in a region of parameter space of great theoretical and phenomenological interest.

Contents

1 Introduction

The development of the Standard Model of particle interactions is the culmination of a century of searches and analysis with fixed-target and colliding beam experiments. Interactions with new forces beyond the Standard Model are currently limited by well-tested gauge symmetries to a handful of possibilities. The only remaining way for interactions with new sub-GeV vector-like forces to arise is for charged particles to acquire millicharges, ϵe, under these forces. This occurs through a simple and generic mechanism proposed by Holdom [1], in which a new vector particle A'_μ mixes via quantum loops with the Standard Model photon. MeV–GeV masses for the A' gauge boson are particularly well-motivated in this context. Such sub-GeV forces are a common feature of extensions of the Standard Model, but existing constraints are remarkably weak, with limits at $\epsilon e \lesssim (0.3-1)\times 10^{-2}e$.

Modern high-intensity fixed-target beams and existing precision spectrometers are ideally suited to explore sub-GeV forces by probing reactions in which a new A' vector particle is produced by radiation off an electron beam. The A' decays to an electron and positron pair and appears as a narrow resonance of small magnitude in the invariant mass spectrum. The production rate of $A's$, the luminosity, and the mass resolution attainable at Jefferson Laboratory vastly exceeds what is currently available using colliding electron beam facilities. For these reasons, we propose a dedicated search using Jefferson Laboratory's Continuous Electron Beam Accelerator Facility (CEBAF) and the High Resolution Spectrometers (HRS) in Hall A. The proposed experiment will probe charged particle couplings with new forces as small as $2\times 10^{-4}e$ and masses between 65 MeV and 550 MeV — an improvement by more than two orders of magnitude in cross section sensitivity over all previous experiments.

This experiment is particularly timely in light of a series of recent anomalies from terrestrial, balloon-borne, and satellite experiments that suggest that dark matter interacts with Standard Model particles. Much of this data sharply hints that dark matter is directly charged under a new force mediated by an A' and not described by the Standard Model. Theoretical as well as phenomenological expectations suggest an A' mass $m_{A'} \lesssim 1\,\mathrm{GeV}$ and $\epsilon e \lesssim 10^{-2}e$. Much of this region will be explored with the proposed experiment.

1.1 Brief overview of the proposed experiment

The experiment will measure the invariant mass spectrum of electron-positron pairs produced by electron scattering on a high-Z Tungsten wire mesh target. The spectrum will be scanned in the wide mass range of 65 MeV to 550 MeV for a narrow peak with a width corresponding to the instrumental resolution. Using single-arm distributions, the acceptance of the experiment will be precisely determined. The electron and positron will be detected in the magnetic spectrometers. For the mass range of interest, the spectrometer will be positioned at small angles, which can be achieved using the recently constructed septum magnet [2]. The relative mass resolution will be 0.5%, limited by multiple scattering in the target material.

The central angle for spectrometers with nominal target position will be 5° as for the ^{208}Pb Radius Experiment (PREX). We plan to move the target along the beam to realize two settings with 4.5° and 5.5° central angles, and use an additional setting at 5° to 6° to cover larger invariant masses. The e^+e^- pairs will be detected in coincindence within a timing window of 20 ns. The rejection of pion backgrounds will be done online by using the Gas Cherenkov counters. With a beam of 80 μA on 0.5%–10% radiation-length targets at

various beam energies, we expect to collect true coincidence e^+e^- events with a rate in the range 100–500 Hz. The total e^+e^- sample size will exceed 10^8 pairs in a 6-day period for each setting. Each kinematic setting will cover an $\mathcal{O}(1)$ interval of the e^+e^- invariant mass range.

We propose a run plan for the 12 GeV running period, using a setting with beam energy 2.2 GeV for 6 days and setting with beam energy 4.4 GeV for 12 days. We additionally propose to use 6 days at 1.1 GeV and 3.3 GeV. We emphasize that this experiment is ready to run anytime, since the special equipment (a wire target) can be ready within a month.

1.2 The impact of this experiment

The proposed experiment will be sensitive to new gauge bosons with couplings as small as $\alpha'/\alpha \sim (6-8)\times 10^{-8}$ for masses in the range $65 - 300\,\mathrm{MeV}$, and couplings as small as $\alpha'/\alpha \sim 2\times 10^{-7}$ for larger $m_{A'} \lesssim 525$ MeV. This is about a factor of $\sim 3-35$ times lower in ϵ than existing constraints (which assume that the A' couples also to muons), and corresponds to $\sim 10 - 1000$ times smaller cross-sections.

This parameter range is interesting for several reasons. This region of mass and coupling is compatible with A''s explaining the annual modulation signal seen by the dark matter direct detection experiment DAMA/LIBRA, and also with dark matter annihilating into A''s, which explains a myriad of recent cosmic-ray and other astrophysical anomalies (see §2.2). In addition, and independently of any connection to dark matter, the proposed experiment would be the first to probe A's of mass $\sim 100\,\mathrm{MeV}$ with gauge kinetic mixing below $\epsilon \sim 10^{-3}$, the range most compatible if the Standard Model hypercharge gauge group is part of a Grand Unified Theory.

The importance for fundamental physics of discovering new forces near the GeV scale cannot be overstated.

1.3 The organization of this proposal

The proposal is organized as follows. In §2, we present the physics of hypothetical A' particles, motivation for its existence, and limits from existing data. In §3, we describe A' production in fixed-target experiments. In §4, we describe the experimental approach, including the standard equipment and the specialized target required for this experiment. In §5, we present the parametrics and the Monte Carlo (MC) simulations of the QED e^+e^- pair production rate and the A' signal rate in the proposed setup. We also describe how we made the sensitivity plots. Other background rates, such as π^+ or e^+ singles and accidental e^+e^- pairs, are discussed in §6. In §7, a description of the experimental concept and the operation of the spectrometer detector system is presented. We will also address the calibration of the spectrometer optics and the acceptance. The expected results and requested beam time are discussed in §8. Technical considerations related to the equipment and a suggested experimental schedule are discussed in §9. The proposal is summarized in §10. Three appendices discuss the form factors used to calculate the signal and background rates (§A), the mass resolution (§B), and the validation of the rates we obtain with the various MC simulations (§C).

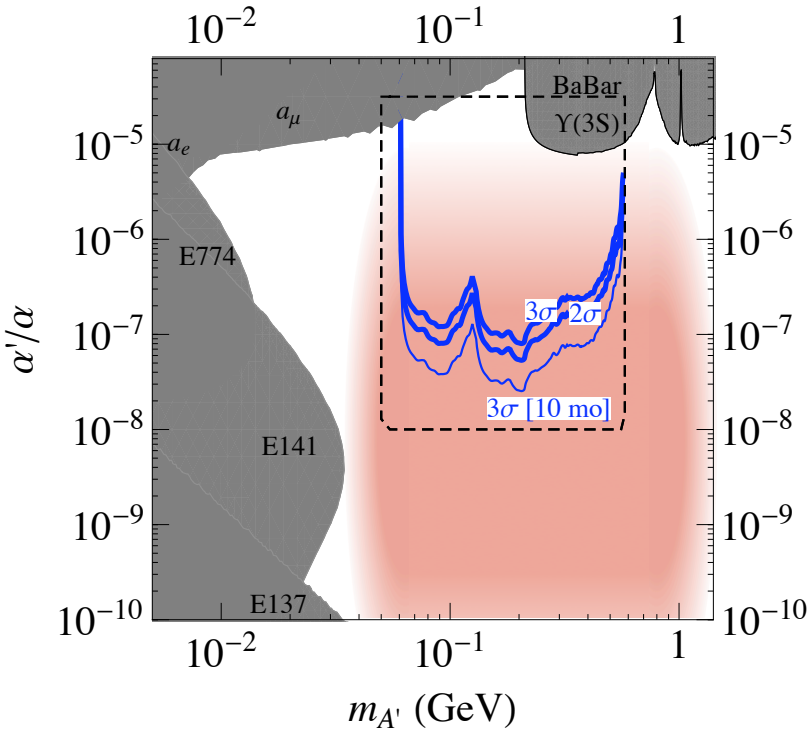

Figure 1: Anticipated 2σ sensitivity for the proposed experiment (thick blue line), with existing constraints on an A' from electron and muon anomalous magnetic moment measurements, a_e and a_μ (see [3]), the BaBar search for $\Upsilon(3S) \to \gamma\mu^+\mu^-$ [4], and three beam dump experiments, E137, E141, and E774 [5, 6, 7] (see [8]). The a_μ and $\Upsilon(3S)$ limits assume equal-strength couplings to electrons and muons. The red region indicates the region of greatest theoretical interest, as described in the text. The gray dashed line indicates the scale used for other plots in this paper.

2 Physics

We propose to search for new sub-GeV mass vector bosons — 'dark photons', A' — that couple very weakly to electrons. It is useful to parameterize the coupling g' of the A' to electrons by a dimensionless $\epsilon \equiv g'/e$, where e is the electron charge. Cross-sections for A' production then scale as $\alpha'/\alpha = \epsilon^2$, where $\alpha' = g'^2/(4\pi)$ and $\alpha = e^2/(4\pi)$ are the fine-structure constants for the dark photon and ordinary electromagnetic interactions. This experiment will search for A' bosons with mass $m_{A'} \sim 65$ MeV – 550 MeV and $\alpha'/\alpha \gtrsim 6 \times 10^{-8}$, which can be produced by a reaction analogous to photon bremsstrahlung (see §3) and decays promptly to e^+e^- or other charged particle pairs. We refer the reader to Figure 1 for a summary of the reach of this experiment.

2.1 Motivation for New Physics Near the GeV Scale

New light vector particles, matter states, and their associated interactions are ubiquitous in extensions of the Standard Model [1, 9, 10, 11, 12, 13]. However, the symmetries of the Standard Model restrict the interaction of ordinary matter with such new states. Indeed,

most interactions consistent with Standard Model gauge symmetries and Lorentz invariance have couplings suppressed by a high mass scale. One of the few unsuppressed interactions is the coupling of charged standard model particles ψ

$$\delta\mathcal{L} = g' A'_\mu \bar{\psi}\gamma^\mu \psi \tag{1}$$

to a new gauge boson A', which is quite poorly constrained for small g' (see Figure 1)[8]. Similar couplings between the A' and other Standard Model fermions are also allowed, with relations between their couplings (anomaly cancellation) required for the A' gauge symmetry to be quantum-mechanically consistent. For example, the A' can couple only to electrons and muons, with opposite charges $g'_e = -g'_\mu$ (a $U(1)_{e-\mu}$ boson), or can have couplings proportional to the electromagnetic charges of each fermion, $g_i = \epsilon e q_i$.

The A' coupling to Standard Model matter can be *induced* by ordinary electromagnetic interactions through the kinetic mixing interaction proposed by Holdom [1],

$$\delta\mathcal{L} = \frac{\epsilon_Y}{2} F'_{\mu\nu} F_Y^{\mu\nu}, \tag{2}$$

where $F'_{\mu\nu} = \partial_\mu A'_\nu - \partial_\nu A'_\mu$ is the field strength of the A' gauge boson, and similarly $F_Y^{\mu\nu}$ is the hypercharge field strength. This effect is generic, ensures that the A' interactions respect parity, and (as we discuss below) naturally produces small g' and A' masses near the GeV scale. This mixing is equivalent in low-energy interactions to assigning a charge $\epsilon e q_i$ to Standard Model particles of electromagnetic charge q_i, where $\epsilon = \epsilon_Y/(\cos\theta_W)$ and θ_W is the Weinberg mixing angle. The A' couplings to neutrinos and parity-violating couplings are negligible compared to Z-mediated effects (see e.g. [14]).

As noted in [1], a new gauge boson A' that does not couple to Standard Model matter at a classical level can still couple through quantum-mechanical corrections. For example, loops of any particle X that couples to both the A' and Standard Model hypercharge generates mixing of the form (2), with

$$\epsilon \sim 10^{-3} - 10^{-2} \qquad (\alpha'/\alpha \sim 10^{-6} - 10^{-4}). \tag{3}$$

These quantum effects are significant regardless of the mass m_X of the particle in question, which could be well above the TeV scale (or even at the Planck scale) and thus evade detection.

Smaller ϵ are expected if nature has enhanced symmetry at high energies. For example, it has been conjectured that the strong and electroweak gauge groups of the Standard Model are embedded in a grand unified theory (GUT) with gauge group $SU(5)$ or larger that is broken spontaneously at a high scale $M_G \approx 10^{16}$ GeV. In this case the mixing (2) is suppressed,

$$\epsilon_{GUT} \sim \frac{\alpha_i^2}{16\pi^2} \ln\left(M_G/M_X\right) \sim 10^{-5} - 10^{-3}, \tag{4}$$

where α_i are gauge couplings. ϵ of this size leads to effective couplings

$$\alpha'/\alpha \sim 10^{-8} - 10^{-6}. \tag{5}$$

As shown in Figure 1, *no experiment to date has probed the range of ϵ expected in grand unified theories for $m_{A'} \gtrsim 50$ MeV.*

An A' mass near but beneath the weak scale is particularly well-motivated, as $U(1)'$ symmetry-breaking and the resulting A' mass may be determined by the same physics that generates the W and Z masses [15]. The best candidate for the origin of the weak scale is low-energy supersymmetry. In this case, the A' can naturally acquire mass suppressed by a loop factor or by $\sqrt{\epsilon}$ compared to the weak scale, leading to MeV to GeV-scale A' masses [9, 15, 16, 17, 18, 14]. In supersymmetric models, the gauge kinetic mixing (2) is accompanied by quartic interactions

$$\delta\mathcal{L} \sim \frac{\epsilon_Y}{4} g_Y g_D |\phi_D|^2 |h|^2, \tag{6}$$

between the Standard Model Higgs doublet h and any scalar ϕ_D charged under $U(1)'$, where g_Y and g_D are the gauge couplings of Standard Model hypercharge and the A' coupling to ϕ_D, respectively. Electroweak symmetry breaking gives h a weak-scale vacuum expectation value, so that (6) generates a mass term for ϕ_D. For positively charged ϕ_D, and sufficiently small bare mass, this mass term is negative and triggers $U(1)'$ breaking by the Higgs mechanism. The resulting induced mass for the A' is

$$m_{A'} \sim \sqrt{\epsilon}\sqrt{\frac{g_D g_Y}{g_2^2}}\, m_W \sim \text{MeV–GeV}, \tag{7}$$

where g_2 is Standard Model $SU(2)_L$ gauge coupling and m_W is the W-boson mass. The resulting mass is precisely in the $50 - 1000$ MeV range targeted by this experiment. Given our ϵ sensitivity, we expect to probe the portion of this parameter space with small g_D. For example, for $g_D \sim 0.04$ and $\epsilon \sim 5 \times 10^{-4}$ ($\alpha'/\alpha \sim 2.5 \times 10^{-7}$), we have $m_{A'} \sim 400$ MeV, which can definitively be probed by the proposed experiment. Note that the mechanism of $U(1)'$ breaking above does not rely on supersymmetry, as any quartic interaction of the form (6), with arbitrary coupling, can transmit electro-weak masses to the A'. Thus, the mass relation (7) should not be interpreted too literally.

We stress that the mass of the A' breaks any apparent symmetry between it and the photon: though Standard Model particles have induced ϵ-suppressed charges under the A', any new matter charged under the A' would *not* have any effective coupling to the photon, and would have gone undetected.

The Hall A HRS is ideally suited to explore the A' parameter space. An electron beam scattering on a high-Z target such as Tungsten will produce A''s through bremsstrahlung reactions with a cross-section

$$\sigma_{A'} \;\sim\; 100 \text{ pb} \left(\frac{\epsilon}{10^{-4}}\right)^2 \left(\frac{100\,\text{MeV}}{m_{A'}}\right)^2, \tag{8}$$

several orders of magnitude larger than in colliding electron and hadron beams [19]. The A' can decay to electrons, and is therefore visible as a narrow resonance in the trident e^+e^- mass spectrum.

Such a new gauge boson would constitute the first discovery of a new gauge force since the observation of Z-mediated neutral currents. Besides the obvious physical interest of a fifth force, the A' like the Z could open up a new "sector" of light, weakly coupled particles whose spectrum and properties could be measured in fixed-target experiments and flavor factories. The A' sector would provide a new laboratory for many physical questions, and would be revealing precisely because its interactions with Standard Model particles are so

weak. In particular, if nature is approximately supersymmetric near the TeV scale, the mass scale of supersymmetry breaking for the A' sector is naturally suppressed by ϵ times gauge couplings. In this case, supersymmetry could be studied easily in the A' sector, and possibly even discovered there by relatively low-energy experiments before Standard Model superpartners are seen at colliders.

2.2 Motivation for an A' from Dark Matter

Dark matter interpretations of recent astrophysical and terrestrial anomalies provide an urgent impetus to search for A''s in the mass range 50 MeV – 1 GeV, with a coupling $\epsilon \sim 10^{-4} - 10^{-2}$.

The concordance model of big bang cosmology — the "Lambda Cold Dark Matter" (ΛCDM) model — explains all observations of the cosmic microwave background, large scale structure formation, and supernovae. This model suggests that Standard Model particles make up only about 4% of the energy density in the Universe, while "dark energy" and "dark matter" make up 74% and 22%, respectively, of the Universe's energy density. The concordance model does not require dark matter to have any new interactions beyond gravity with Standard Model particles. However, an intriguing theoretical observation, dubbed the *WIMP miracle*, suggests that dark matter *does* have new interactions. In particular, if dark matter consists of ∼100 GeV to 10 TeV particles interacting via the electroweak force ("weakly interacting massive particles" or "WIMPs"), they would automatically have the right relic abundance observed today.

In addition to the WIMP miracle, evidence from cosmic-ray data and the terrestrial direct dark matter detection experiment DAMA/LIBRA strongly suggest that dark matter interacts with ordinary matter *not* just gravitationally. While the WIMP miracle suggests that dark matter is charged under the Standard Model electroweak force, we will see that *these observations provide impressive evidence for dark matter interacting with ordinary matter through a new force, mediated by a new 50 MeV – 1 GeV mass gauge boson.* In addition to explaining any or all of these observations, dark matter charged under this new force automatically has the correct thermal relic abundance observed today by virtue of its interactions via the new force carrier, reproducing the success of the WIMP dark matter hypothesis.

The satellites PAMELA [20] and Fermi [21], the balloon-borne detector ATIC [22], the ground-based telescope HESS [23, 24], as well as other experiments, observe an excess in the cosmic-ray flux of electrons and/or positrons above backgrounds expected from normal astrophysical processes. If their source is dark matter annihilation or decay, synchrotron radiation from these electrons and positrons could also explain the "WMAP haze" near the Galactic center [25], which consists of an excess seen in the WMAP Cosmic Microwave Background data. In addition, starlight near the Galactic center would inverse Compton scatter off the high energy electrons and positrons and produce an excess in gamma-rays. A detection of a gamma-ray excess towards the Galactic center region in the gamma-ray data obtained with the Fermi satellite was recently reported in [26], and has been dubbed the "Fermi haze".

Taken together, these observations by several experimental collaborations provide compelling evidence that there is an unexplained excess in cosmic-ray electrons and positrons in our Galaxy. Given the firm evidence for a 22% dark matter content of the Universe,

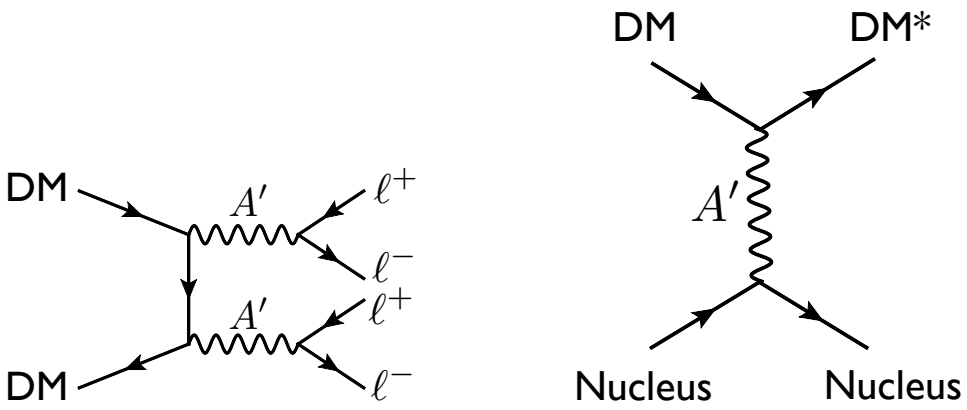

Figure 2: **Left:** Dark matter annihilation into the dark photon A', which decays into charged leptons such as electrons and/or muons, can explain the cosmic-ray electron and/or positron excesses seen by PAMELA, Fermi, ATIC, HESS, and other experiments. **Right:** Dark matter scattering into an excited state off nuclei through A' exchange in direct dark matter detection experiments can explain the annual modulation signal observed by DAMA/LIBRA, and the null results of other direct detection experiments.

a very natural source of these excesses is dark matter annihilation. However, two features of these observations are incompatible with annihilation of ordinary thermal WIMP dark matter. They instead provide impressive evidence that dark matter is charged under a new $U(1)'$ and annihilating into the A', which decays directly into electrons and positrons, or into muons that decay into electrons and positrons, see Figure 2 (left) (see e.g. [27, 28, 29, 30, 31, 32, 33, 34]). These two features are:

- The annihilation cross-section required to explain the signal is 50-1000 times larger than the thermal freeze-out cross-section for an ordinary WIMP that is needed to reproduce the observed dark matter relic density. This can be explained if dark matter interacts with a new long range force mediated by an $\mathcal{O}$(GeV) mass gauge boson, which allows the dark matter annihilation cross-section ($\langle\sigma v\rangle$) to be enhanced at low dark matter velocities, i.e. $\langle\sigma v\rangle \propto 1/v$. In this case, in the early Universe when the dark matter velocity was high ($\sim 0.3c$), the annihilation cross-section that determines the relic abundance can naturally be the same as that of an ordinary WIMP and reproduce the WIMP miracle. However, in the Milky Way halo now, the dark matter has a much lower velocity ($v \sim 10^{-3}c$), leading to a large increase in the annihilation cross-section that is required to explain the cosmic-ray data. The enhancement at low velocities through a new long-range force is very well known and called the Sommerfeld effect [35].

- The PAMELA satellite did *not* see an anti-proton excess [36], which strongly suggests that dark matter annihilation is dominantly producing leptons, and not baryons. If dark matter is interacting via a $\mathcal{O}(GeV)$ mass force particle in order to have a large annihilation rate via the Sommerfeld mechanism, then annihilations into the force carrier automatically fail to produce any baryons. Kinematically, the force carriers cannot

decay into baryons, and are instead forced to decay into the lighter charged leptons. Thus, annihilation products of dark matter are leptonic in this case.

To explain the additional sources of evidence for a new GeV scale force, we briefly summarize the consequence for dark matter mass spectra that follow from dark matter carrying a charge under a new force. If dark matter is charged under a non-Abelian force that acquires mass, then radiative effects can split all components of the dark matter with size, $\delta \sim \alpha_D \Delta m_{W_D}$, where α_D is the non-Abelian fine structure constant and Δm_{W_D} is the splitting of gauge boson masses [27]. Typically, these splittings are $\Delta m_{W_D} \sim \alpha_D m_{W_D} \sim 1 - 10\,\mathrm{MeV}$ for $m_{W_D} \sim 1\,\mathrm{GeV}$ [27]. Thus, $\delta \sim 100$ keV for $\alpha_D \sim 10^{-2}$. These splittings are completely analogous to the splittings that arise between the $\pi^\pm$ and π^0 from Standard Model SU(2) breaking. If instead a non-Abelian force confines at a scale $\Lambda_D \sim$ GeV, then a heavy-flavor meson can be cosmologically long-lived and thus a dark matter candidate [37]. Hyperfine interactions can naturally induce ~ 100 keV splittings of the dark matter particles in this case. We emphasize that the GeV scale force carrier particles mediate quantum corrections that generate the 100 keV and 1-10 MeV splittings of dark matter states [27, 38, 39, 37].

When mass splittings arise, A' mediated interactions of dark matter with ordinary matter as well as dark matter self-interactions are dominated by inelastic collisions [27]. The direct dark matter detection experiment DAMA/LIBRA as well as the INTEGRAL telescope provide intriguing evidence for such interactions. The DAMA/NaI [40] and DAMA/LIBRA [41] experiments have reported an annual modulation signal over nearly eleven years of operation with more than 8σ significance. Modulation is expected because the Earth's velocity with respect to the dark matter halo varies as the Earth moves around the sun, and the phase of the observed modulation is consistent with this origin. A simple hypothesis that explains the spectrum and magnitude of the signal, and reconciles it with the null results of other experiments, is that dark matter-nucleus scattering is dominated by an inelastic process,

$$\chi\, N \to \chi^*\, N, \tag{9}$$

in which the dark matter χ scatters off a nucleus N into an excited state χ^* with mass splitting $\delta \approx 100$ keV [38]. The kinematics of these reactions is also remarkably consistent with all the distinctive properties of the nuclear recoil spectrum reported by DAMA/LIBRA. In addition, the INTEGRAL telescope [42] has reported a 511keV photon signal near the galactic center, indicating a new source of $\sim$ 1-10 MeV electrons and positrons. This excess could be explained by collisions of $\mathcal{O}$(100 GeV-1 TeV) mass dark matter into $\mathcal{O}$(MeV) excited states in the galaxy [43] — dark matter excited by scattering decays back to the ground state by emitting a soft e^+e^- pair. The 511keV excess then arises from the subsequent annihilation of the produced positrons.

The existence of an A' may also help explain various other particle physics anomalies [3] such as the anomalous magnetic moment of the muon ($(g-2)_\mu$) [44] and the HyperCP anomaly [45].

While these experimental hints provide an urgent motivation to look for an A', it is important to emphasize the value of these searches in general. There has never been a systematic search for new GeV-scale force carriers that are weakly coupled to Standard Model particles. Nothing forbids their existence, and their discovery would have profound implications for our understanding of nature. A relatively simple experiment using the

facilities available in Hall A at Jefferson Laboratory will probe a large and interesting range of A' masses and couplings.

2.3 Existing constraints

Constraints on new A''s that decay to e^+e^- and the search reach of an experiment using the spectrometers of Hall A at Jefferson Laboratory are summarized in Figure 1. Shown are constraints from electron and muon anomalous magnetic moment measurements, a_e and a_μ [3], the BaBar search for $\Upsilon(3S) \to \gamma A' \to \gamma\mu^+\mu^-$ [19], and three beam dump experiments, E137, E141, and E774 [8]. The constraints from a_μ and the BaBar search assume that the A' couples to muons — this is the case, for example, if it mixes with the photon. If it only couples to electrons, then the constraints on α'/α and $m_{A'}$ in the region to which the proposed experiment is sensitive are weaker than $\alpha'/\alpha \lesssim 10^{-4}$.

We refer the reader to [8, 3] for details on existing constraints. Here, we briefly review the constraint on $e^+e^- \to \gamma A' \to \gamma\mu^+\mu^-$ derived from the BaBar search [46]. If the A' couples to both electrons and muons, this is the most relevant constraint in the region probed by the proposed experiment. The analysis of [46] was in fact a search for $\Upsilon(3S)$ decays into a pseudoscalar a, $\Upsilon(3S) \to \gamma a \to \gamma\mu^+\mu^-$, but can be interpreted as a limit on A' production because the final states are identical. Using $\mathcal{L}_{\rm int} \sim 30$ fb^{-1} of data containing $\sim 122 \times 10^6$ $\Upsilon(3S)$ events, a 90% C.L. upper limit of roughly $(1-4)\times 10^{-6}$ on the $\gamma\mu^+\mu^-$ branching fraction was found for $m_{A'} \sim 2m_\mu - 1$ GeV. This search would thus be sensitive to about $\sim 100 - 500$ events with $e^+e^- \to \gamma A' \to \gamma\mu^+\mu^-$. Requiring that $\sigma(e^+e^- \to \gamma A') \times BR(A' \to \mu^+\mu^-) \times \mathcal{L}_{\rm int} \lesssim 500$, where $BR(A' \to \mu^+\mu^-) = 1/(2 + R(m_{A'}))$ for $m_{A'} > 2m_\mu$ with $R = \frac{\sigma(e^+e^- \to \text{hadrons};\, E=m_{A'})}{\sigma(e^+e^- \to \mu^+\mu^-;\, E=m_{A'})}$, and rescaling the resulting constraint to represent a 95% C.L. upper bound, we find the constraint depicted in Figure 1. For $m_{A'} \gtrsim 2m_\mu$, this requires $\alpha'/\alpha \gtrsim 10^{-5}$, while the constraint weakens at higher masses, especially near the ρ-resonance.

We caution that systematic uncertainties in the A' limit beyond those quoted in [46] may slightly weaken the resulting limit, which should therefore be taken as a rough approximation unless further analysis is done. First, A' production in B-factories is more forward-peaked than the $\Upsilon(3S)$ decay mode considered in [46], so that the signal acceptance is more uncertain. In addition, background distributions in [46] are derived from smooth polynomial fits to data collected on the $\Upsilon(4S)$ resonance, which is assumed to contain no signal. This assumption is not correct for A' production, though the resulting systematic effects are expected to be small.

2.4 Potential Improvements From Existing Data

Several past and current experiments have data that could be used to significantly improve current limits on α'/α, as discussed in [3, 47]. Here, we estimate the potential sensitivity of searches in three channels ($\pi^0 \to \gamma A' \to \gamma e^+e^-$, $\phi \to \eta A' \to \eta e^+e^-$, and $e^+e^- \to \gamma A' \to \gamma\mu^+\mu^-$), considering only the statistical uncertainties and irreducible backgrounds. These are likely overestimates, as we are unable to include either systematic uncertainties or significant instrumental backgrounds such as photon conversion in the detector volume.

BaBar, BELLE, and KTeV (E799-II) have produced and detected large numbers of neutral pions, of order 10^{10}, of which roughly 1% decay in the Dalitz mode $\pi^0 \to e^+e^-\gamma$. These experiments can search for the decay $\pi^0 \to \gamma A'$ induced by A'–photon kinetic mixing, which

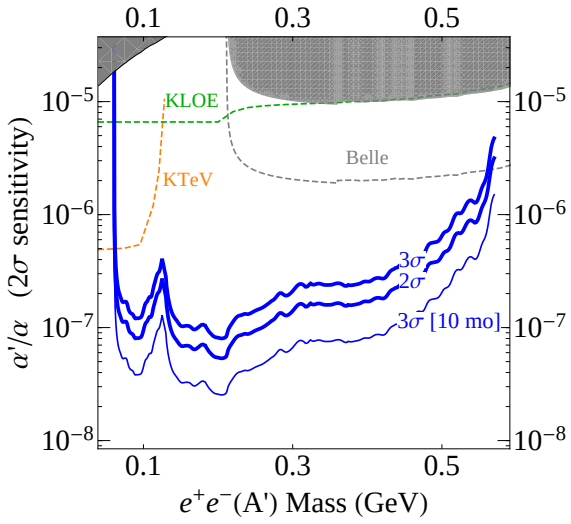

Figure 3: The 2σ sensitivity of the proposed experiment (thick blue line), compared with current limits and estimated potential 2σ sensitivity for A' searches in existing data (dashed lines), assuming optimal sensitivity as described in the text. From left to right: KTeV $\pi^0 \to \gamma A' \to \gamma e^+e^-$ (orange dashed curve), KLOE $\phi \to \eta A' \to \eta e^+e^-$ (green dashed curve) and Belle $e^+e^- \to \gamma A' \to \gamma \mu^+\mu^-$ (gray dashed curve). Existing constraints are as in Figure 1.

would appear as a narrow resonance over the continuum Dalitz decay background. KTeV has the largest π^0 sample, and its e^+e^- mass resolution can be approximated from the reported measurement of the $\pi^0 \to e^+e^-$ branching fraction [48] to be roughly 2 MeV. This paper also reports the measured mass distribution of Dalitz decays above 70 MeV, from which we estimate potential sensitivity to α'/α as small as 5×10^{-7} for $70 < m(e^+e^-) \lesssim 100$ MeV, as shown by the orange shaded region in Figure 3.

Similarly, KLOE can search for the decay $\phi \to \eta A'$, likewise induced by A' kinetic mixing with the photon, in a sample of 10^{10} ϕ's. An analysis of this data is ongoing [49]. We have taken the blue dashed curve in Figure 3 from [47], which assumes that mass resolution σ_m is dominated by KLOE's 0.4% momentum resolution. We have adjusted the contours from [47] to determine a 2σ contour and enlarged the bin width used to determine signal significance from σ_m in [47] to $2.5\sigma_m$. Above the muon threshold, ϕ decays are not competitive with B-factory continuum production.

In addition, BaBar and Belle can search for the continuum production mode $e^+e^- \to \gamma A' \to \gamma \mu^+\mu^-$ in their full datasets. For example, an analysis of the Belle $\Upsilon(4S)$ data set would increase statistics by a factor of ~ 24 relative to the BaBar $\Upsilon(3S)$ search that we have interpreted as a limit above. We have derived the expected sensitivity (shown as a black dashed line in Figure 3) simply by scaling the $\Upsilon(3S)$ estimated reach by $\sqrt{24}$. These searches have not been extended below the muon threshold because of large conversion backgrounds.

3 The production of an A' in fixed target collisions

A' particles are generated in electron collisions on a fixed target by a process analogous to ordinary photon bremsstrahlung, see Figure 4. This can be reliably estimated in the

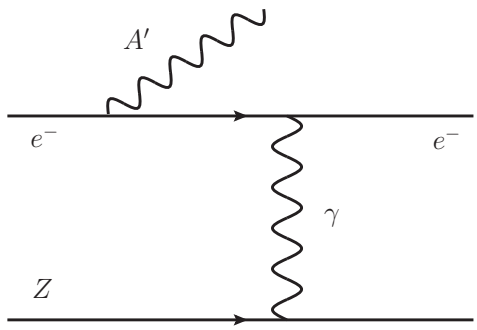

Figure 4: A' production by bremsstrahlung off an incoming electron scattering off protons in a target with atomic number Z.

Weizsäcker-Williams approximation (see [8, 50, 51, 52]). When the incoming electron has energy E_0, the differential cross-section to produce an A' of mass $m_{A'}$ with energy $E_{A'} \equiv xE_0$ is

$$\frac{d\sigma}{dx d\cos\theta_{A'}} \approx \frac{8Z^2\alpha^3\epsilon^2 E_0^2 x}{U^2}\tilde{\chi} \times \left[(1-x+\frac{x^2}{2}) - \frac{x(1-x)m_{A'}^2\,(E_0^2 x\,\theta_{A'}^2)}{U^2}\right] \tag{10}$$

where Z is the atomic number of the target atoms, $\alpha \simeq 1/137$, $\theta_{A'}$ is the angle in the lab frame between the emitted A' and the incoming electron,

$$U(x,\theta_{A'}) = E_0^2 x\theta_{A'}^2 + m_{A'}^2\frac{1-x}{x} + m_e^2 x \tag{11}$$

is the virtuality of the intermediate electron in initial-state bremsstrahlung, and $\tilde{\chi} \sim 0.1-10$ is the Weizsäcker-Williams effective photon flux, with an overall factor of Z^2 removed. The form of $\tilde{\chi}$ and its dependence on the A' mass, beam energy, and target nucleus are discussed in Appendix A. The above results are valid for

$$m_e \ll m_{A'} \ll E_0, \qquad x\,\theta_{A'}^2 \ll 1. \tag{12}$$

For $m_{A'} \gg m_e$, the angular integration gives

$$\frac{d\sigma}{dx} \approx \frac{8Z^2\alpha^3\epsilon^2 x}{m_{A'}^2}\left(1+\frac{x^2}{3(1-x)}\right)\tilde{\chi}. \tag{13}$$

The rate and kinematics of A' radiation differ from massless bremsstrahlung in several important ways:

Rate: The total A' production rate is controlled by $\frac{\alpha^3\epsilon^2}{m_{A'}^2}$. Therefore, it is suppressed relative to photon bremsstrahlung by $\sim \epsilon^2\frac{m_e^2}{m_{A'}^2}$. Additional suppression from small $\tilde{\chi}$ occurs for large $m_{A'}$ or small E_0.

Angle: A' emission is dominated at angles $\theta_{A'}$ such that $U(x,\theta_{A'}) \lesssim 2\,U(x,0)$ (beyond this point, wide-angle emission falls as $1/\theta_{A'}^4$). For x near its median value, the cutoff emission angle is

$$\theta_{\mathrm{A'\,max}} \sim \max\left(\frac{\sqrt{m_{A'}m_e}}{E_0}, \frac{m_{A'}^{3/2}}{E_0^{3/2}}\right), \tag{14}$$

which is parametrically smaller than the opening angle of the A' decay products, $\sim m_{A'}/E_0$. Although this opening angle is small, the backgrounds mimicking the signal (discussed in §6) dominate at even smaller angles.

Energy: A' bremsstrahlung is sharply peaked at $x \approx 1$, where $U(x,0)$ is minimized. When an A' is produced, it carries nearly the entire beam energy — in fact the median value of $(1-x)$ is $\sim \max\left(\frac{m_e}{m_{A'}}, \frac{m_{A'}}{E_0}\right)$.

The latter two properties are quite important in improving signal significance, and are discussed further in §6.

Assuming the A' decays into Standard Model particles rather than exotics, its boosted lifetime is

$$\ell_0 \equiv \gamma c\tau \simeq \frac{3E_{A'}}{N_{\rm eff} m_{A'}^2 \alpha \epsilon^2} \simeq \frac{0.8{\rm cm}}{N_{\rm eff}} \left(\frac{E_0}{10{\rm GeV}}\right)\left(\frac{10^{-4}}{\epsilon}\right)^2\left(\frac{100\,{\rm MeV}}{m_{A'}}\right)^2, \tag{15}$$

where we have neglected phase-space corrections, and $N_{\rm eff}$ counts the number of available decay products. If the A' couples only to electrons, $N_{\rm eff} = 1$. If the A' mixes kinetically with the photon, then $N_{\rm eff} = 1$ for $m_{A'} < 2m_\mu$ when only $A' \to e^+e^-$ decays are possible, and $2 + R(m_{A'})$ for $m_{A'} \geq 2m_\mu$, where $R = \frac{\sigma(e^+e^- \to \text{ hadrons};\, E=m_{A'})}{\sigma(e^+e^- \to \mu^+\mu^-;\, E=m_{A'})}$ [53]. For the ranges of ϵ and $m_{A'}$ probed by this experiment, the mean decay length $\ell_0 \lesssim 250\mu$m is not significant, but the ability to cleanly reconstruct vertices displaced forward by a few cm would open up sensitivity to considerably lower values of ϵ.

The total number of A' produced when N_e electrons scatter in a target of $T \ll 1$ radiation lengths is

$$N \sim N_e \frac{N_0 X_0}{A} T \frac{Z^2\alpha^3\epsilon^2}{m_{A'}^2} \tilde{\chi} \sim N_e \mathcal{C}\, T\, \epsilon^2 \frac{m_e^2}{m_{A'}^2}, \tag{16}$$

where X_0 is the radiation length of the target in g/cm^2, $N_0 \simeq 6 \times 10^{23}\,{\rm mole}^{-1}$ is Avogadro's number, and A is the target atomic mass in g/mole. The numerical factor $\mathcal{C} \approx 5$ is logarithmically dependent on the choice of nucleus (at least in the range of masses where the form-factor is only slowly varying) and on $m_{A'}$, because, roughly, $X_0 \propto \frac{A}{Z^2}$ (see [8] and [53]). For a Coulomb of incident electrons, the total number of A''s produced is given by

$$\frac{N}{\rm C} \sim 10^6 \tilde{\chi} \left(\frac{T}{0.1}\right)\left(\frac{\epsilon}{10^{-4}}\right)^2\left(\frac{100\,{\rm MeV}}{m_{A'}}\right)^2. \tag{17}$$

The spectrometer efficiency can be estimated from Monte Carlo simulation of the signal, discussed in §5. It is quite low, but of course depends on the precise spectrometer settings. For example, for $m_{A'} = 200$ MeV, $E_0 = 3.056$ GeV, an angular acceptance window of $\theta_x = 0.055 - 0.102$ rad and $|\theta_y| \leq 0.047$ rad (corresponding to an HRS central angle of 4.5°) and a momentum acceptance of $E = 1.452 - 1.573$ GeV for both the positron and one of the electrons, gives a spectrometer efficiency of $\sim 0.14\%$.

4 Experimental setup

The proposed experiment will study e^+e^- production off an electron beam incident on a high-Z target as illustrated in Figure 5. The beam will pass through a tungsten wire

mesh plane tilted by 0.5° with respect to the beam direction. The beam will be rastered in both directions: horizontally by ±0.25 mm and vertically by ±2.5 mm. The e^+e^- pair components will be detected in the HRS spectrometers. The detector package in each HRS includes two vertical drift chambers (VDC), the single PMT trigger scintillator counter, the Gas Cherenkov counter, the segmented high-resolution scintilator hodoscope, and the double-layer lead-glass shower counter.

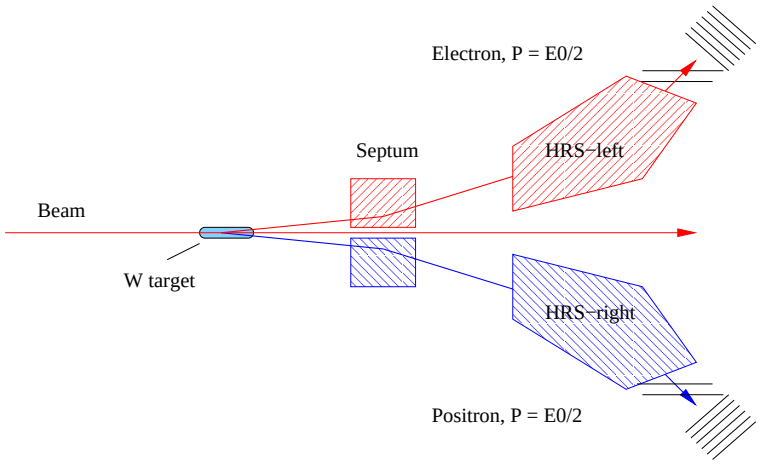

Figure 5: The layout of the experimental setup.

4.1 The radiation budget

Based on experience with the PREX tests, an incident electron beam with an intensity of up to 110 μA on a lead target of thickness 10% (radiation length) in Hall A is feasible, and will not produce too much radiation.

4.2 The long tilted target

The experiment will utilize the standard Hall A scattering chamber as it is used by the PREX experiment, with a target consisting of a 50-cm-long tilted wire mesh plane. The concept of the target is presented in Figure 6. The wires comprising each plane are perpendicular to the beam-line. The tilt angle of 10 mrad is sufficient to ensure stability of the beam-target geometry, and at the same time such a tilt angle is 10 times smaller than the central angle to the HRS, which results in a reduction of the path length traversed by the produced e^+e^- pairs. The wires comprising the foil are spaced so that outgoing e^+e^- pairs only travel through a single wire. For wire thickness of $\sim 10^{-3}$ radiation lengths, this considerably reduces the multiple scattering in the target versus that in a true foil and leads to a much better mass resolution. The maximum number of wires that a beam electron can pass through per plane is 7 in the configuration illustrated in Figure 6 assuming $10\mu m$ diameter tungsten wires. Wires as thick as $15\mu m$ can be used without significantly compromising mass resolution. The plane of the target wire mesh will be vertical. The mesh plane will have 4–5 zig-zags, each with length $5-10$ cm, which result in multiple intersection points allowing an extra factor of 4–5 for rejection of accidental tracks in offline analysis.

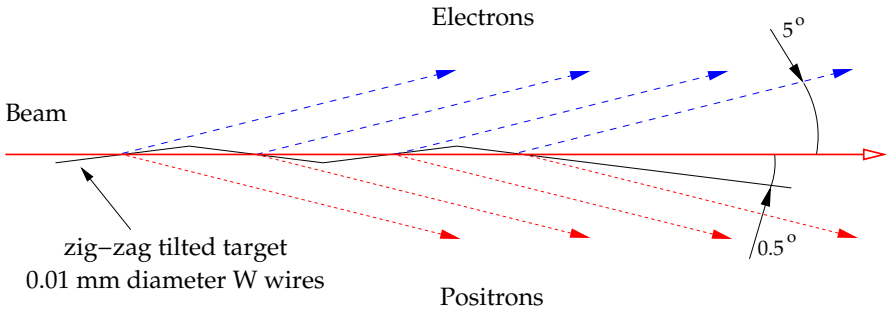

Figure 6: The top view of the tilted target. The beam is rastered over an area 0.5×5 mm^2 (the latter is in the vertical direction). The beam intersects the target in four areas spread over almost 500 mm. Pair components will be detected by two HRS spectrometers at a central angle of ±5°. Each zig-zag of the target plane is tilted with respect to the beam by 0.5°.

The central angle of the spectrometer varies with the position of the target, see Figure 7. In this experiment such variation is very useful because it extends the range of invariant mass covered with one setting of the spectrometers. For several settings suggested in our run plan, only two planes of wire mesh are needed, one at the front and back of the acceptance region.

There are two considerations to take into account when selecting the material. The first consideration is to achieve the highest possible ratio of signal to background, while keeping the background rate low enough so as not to overwhelm the triggering and data acquisition (DAQ) system. The second is whether a thin foil or a thin wire of a particular material is available. Large backgrounds come from pions produced in photo-production from nucleons, and from electrons produced in the radiative tail of electron-proton elastic scattering. These backgrounds do not mimic the signal, but if their rate is too large, they can overwhelm the DAQ system. These considerations favor the use of a tungsten target, with a total thickness between 0.5% and 10% radiation length, with thicker targets used in higher-energy runs. Reduction of the thickness at low energies is required to limit the rate in the electron spectrometer and also minimizes the multiple-scattering contribution to the pair mass resolution.

4.3 The room temperature septum magnet

The septum magnet (see Figure 8) was recently constructed and tested and will be used for the PREX experiment with a 100 μA beam and a thick Pb target. This magnet allows one to change the direction of the field independently in the apertures for the two spectrometers.

4.4 The detector package

The detector packages of the two spectrometers are designed to perform various functions in the characterization of charged particles passing through the spectrometer. The components of the packages are shown in Figure 9. These include: providing a trigger to activate the DAQ

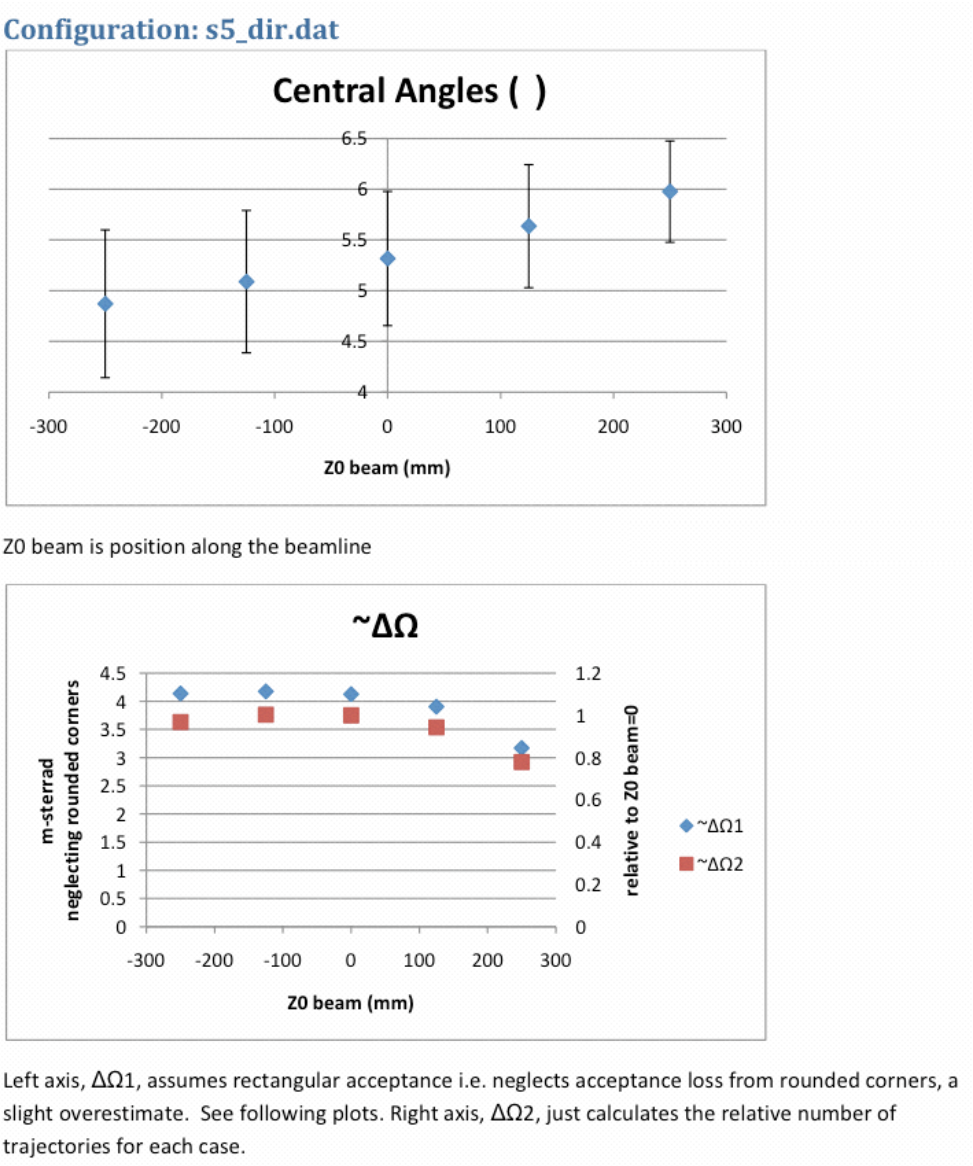

Figure 7: The results of a Monte-Carlo study of the HRS angular acceptance with the septa magnet for different positions of the target along the beam direction.

electronics, collecting tracking information (position and direction), precise timing for time-of-flight measurements and coincidence determination, and identification of the scattered particles. The timing information is provided from scintillators, as well as the main trigger. The particle identification is obtained from a variety of Cherenkov type detectors (aerogel and gas) and lead-glass shower counters. A pair of VDCs provides tracking information. The main part of the detector package in the two spectrometers (trigger scintillators and VDCs) is identical; the arrangement of particle-identification detectors differs slightly. The optics of the HRS spectrometers results in a narrow distribution of particle trajectories in the transverse direction, leading to an aspect ratio of the beam envelope of about 20:1 at the beginning of the detector package and 4:1 at the end.

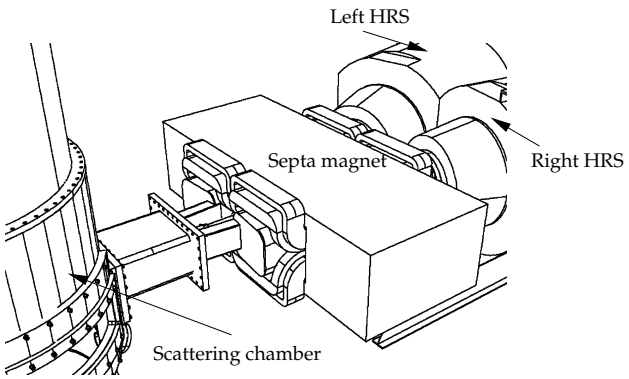

Figure 8: The drawing of the PREX setup with the septa magnet in front of the HRS spectrometers.

The detector package and all DAQ electronics are located inside a Shield Hut (SH) to protect the detector against radiation background. Figure 9 shows side views of the detector setup for the two HRS's, including the movable frame, the detector stack and the DAQ electronics.

4.5 Trigger and DAQ configurations

The main trigger for this experiment is given by a coincidence between signals from the two arms. The coincidence will be formed by two independent logic schemes, one with a timing window of 20 ns between the signals of the S0 scintillator counters (S0-Negative and S0-Positive) and a 40 ns time interval between the scintillator counter signals and the Gas Cherenkov counter of the positron arm, and a second with a timing window of 100 ns. The second signal will be prescaled by a factor 20. Most of the DAQ rate will come from events with a coincident electron and positron within a 20 ns time interval.

4.6 HRS optics quality

The following results were obtained from elastic scattering data taken at $E_0 = 2000$ MeV on a thin ^{12}C target with the vacuum coupling between the scattering chamber and the HRS. An example of a momentum spectrum obtained with the septa magnet and 6° degree scattering angle is shown in Figure 10. The full width at half maximum is 1×10^{-4}, which is in agreement with the HRS design parameters.

The angle reconstruction parameters will be calibrated by using the well developed method of a sieve slit. An example of the optics pattern is shown in Figure 11.

The accuracy of the angle reconstruction inside the spectrometer aceptance relative to the central angle have been usually done on the level of 0.2 mrad. The absolute calibration of the central angle of the spectrometer requires an additional consideration. In this experiment the sieve slits will be mounted in front of the septum magnet, and the distance between central holes in two sieves will be measured with 25-50 μm accuracy. The uncertainty in the beam position to the first order does not contribute to the determination of the sum of the central angles. The accuracy of the sum of the central angle measurement is expected to be on the level of 0.1 mrad or better.

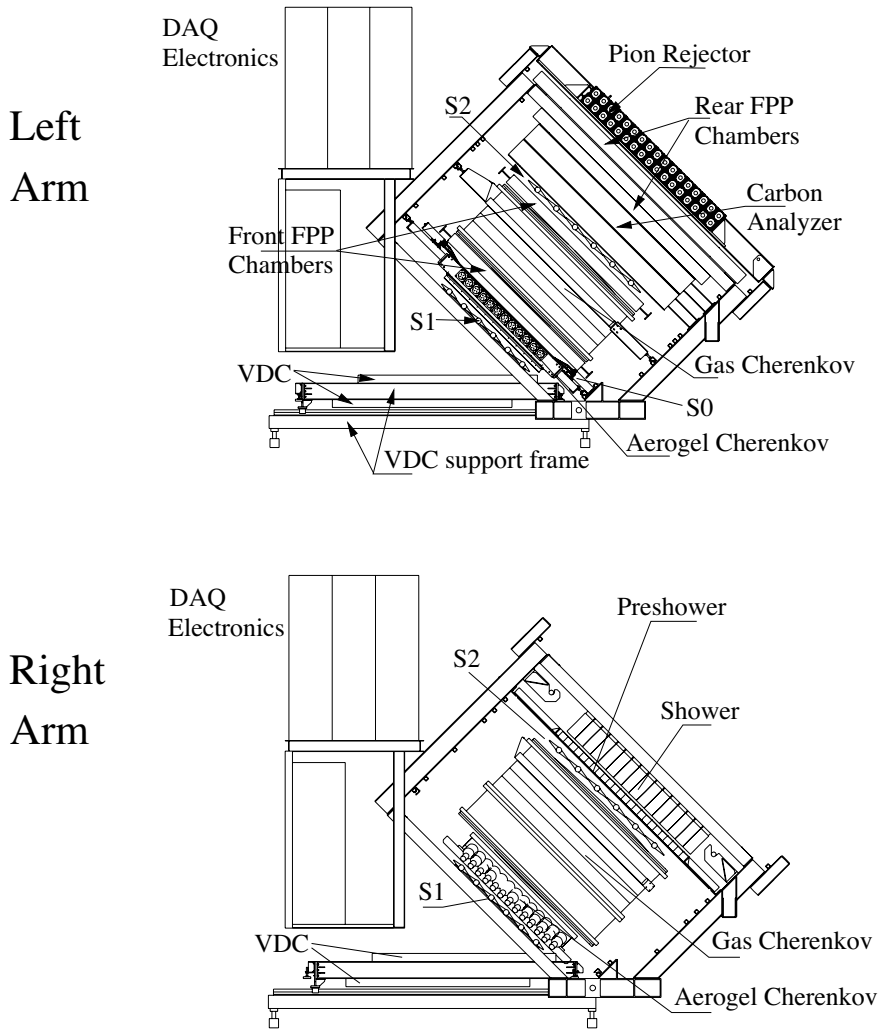

Figure 9: Sideview of detector stack for the HRS. Individual elements of the detector system are indicated in the configuration used most frequently. Also shown is the position of the data-acquisition (DAQ) electronics and of the VDC support frame.

4.7 Parameters of the HRS

A complete description of the Hall A instrumentation was published in NIM-A article [54], from which we obtain the information in Table 1.

These parameters correspond to a point target and do not include the effects of multiple scattering in the target and windows. In the calculation of the invariant mass resolution the effect of multiple scattering in the target was taken into account. The vacuum coupling of

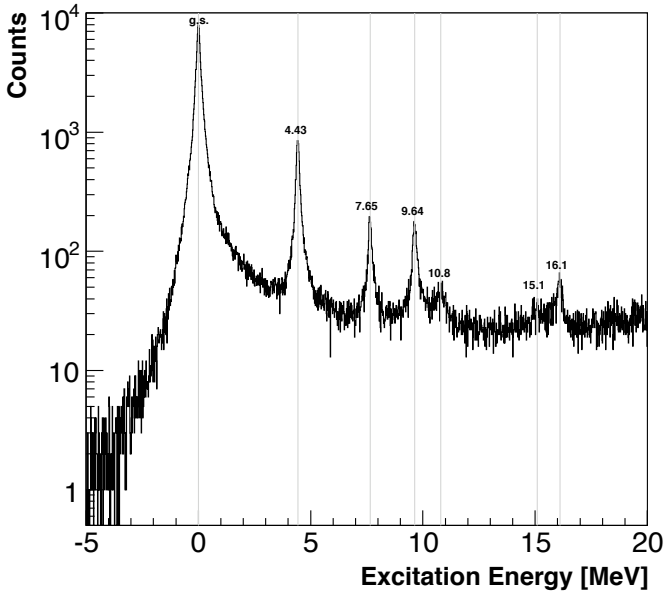

Figure 10: The momentum of the scattered electron in the ^{12}C(e, e') reaction, indicating a FWHM of 1×10^{-4} (relative). The beam energy was 2000 MeV, the scattering angle 6°.

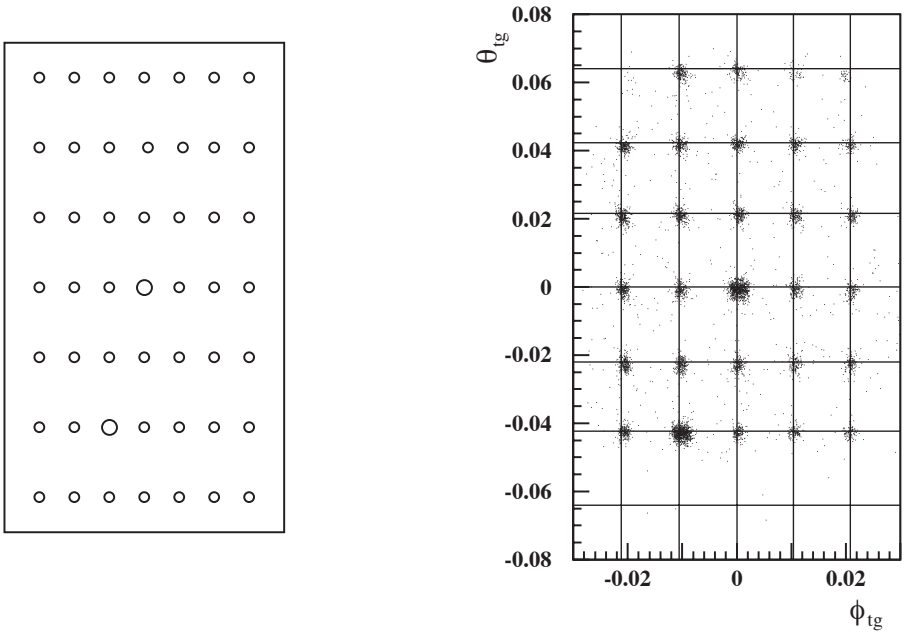

Figure 11: Geometric (left) and reconstructed (right) configurations of the sieve slit. The large holes, which allow for an unambiguous identification of the orientation of the image at the focal plane, can be clearly identified in the right figure.

the scattering chamber and the spectrometer allows one to avoid using windows.

Table 1: Main design characteristics of the Hall A High Resolution Spectrometers at nominal target position. The resolution values are for the FWHM.

Configuration	QQD$_n$Q Vertical bend
Bending angle	45°
Optical length	23.4 m
Momentum range	0.3 - 4.0 GeV/c
Momentum acceptance	-4.5% < δp/p <+4.5%
Momentum resolution	1×10^{-4}
Dispersion at the focus (D)	12.4 m
Radial linear magnification (M)	-2.5
D/M	5.0
Angular range HRS-L	12.5° - 150°
HRS-R	12.5° - 130°
Angular acceptance: Horizontal	±30 mrad
Vertical	±60 mrad
Angular resolution : Horizontal	0.5 mrad
Vertical	1.0 mrad
Solid angle at δp/p = 0, y$_0$ = 0	6 msr
Transverse length acceptance	±5 cm
Transverse position resolution	1 mm

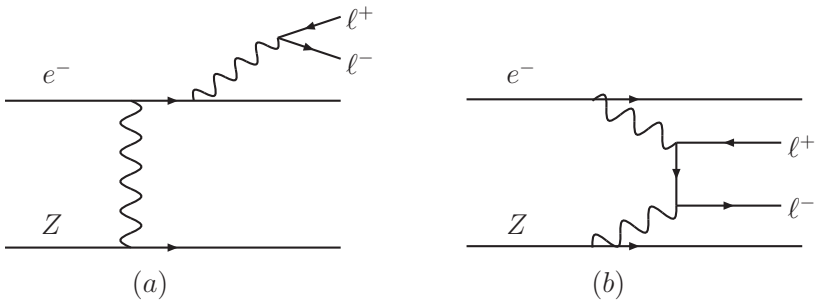

Figure 12: Sample diagrams of (a) radiative trident (γ^*) and (b) Bethe-Heitler trident reactions that comprise the primary QED background to $A' \to \ell^+\ell^-$ search channels.

5 Signal and Trident Kinematics

The stark kinematic differences between QED trident backgrounds and the A' signal are the primary considerations in determining the momentum settings of the spectrometers. As we will show in §6, QED tridents dominate the final event sample after offline rejection of accidentals, so we consider their properties in some detail here.

The irreducible background rates are given by the diagrams shown in Figure 12. These trident events can be usefully separated into "radiative" diagrams (Figure 12(a)), and "Bethe-Heitler" diagrams (Figure 12(b)), that are separately gauge-invariant.

We have simulated the production of these continuum trident background events in QED

using the nuclear elastic and inelastic form-factors in [50]. The simulation is done using MadGraph and MadEvent [55] to compute the matrix elements for $e^-Z \to e^- (e^+e^-) Z$ exactly, but neglecting the effect of nuclear excitations on the kinematics in inelastic processes. The MadEvent code was modified to properly account for the masses of the incoming nucleus and electron in event kinematics, and the nucleus is assumed to couple with a form-factor G_2 defined in Appendix A.

The continuum trident background was simulated including the full interference effects between the diagrams in Figure 12. In addition, a "reduced-interference" approximation simplifies the analysis and is much less computationally intensive. In this approximation, we treat the recoiling e^- and the e^- from the produced pair as distinguishable. Furthermore, we separate trident processes into the radiative diagrams (Figure 12(a)) and the Bethe-Heitler diagrams (Figure 12(b)), and we calculate the cross-section for both of these diagrams separately. This approximation under-estimates the background rates by a factor of about 2–3 in the range of A' masses and beam energies considered in this proposal. For the reach analysis discussed below, we have used differential distributions computed in the "reduced-interference" approximation, then rescaled to the cross-section for the full-interference process.

The contribution from the radiative diagrams (Figure 12(a)) alone is also useful as a guide to the behavior of A' signals at various masses. Indeed, the kinematics of the A' signal events is identical to the distribution of radiative trident events restricted in an invariant mass window near the A' mass. Moreover, the rate of the A' signal is simply related to the radiative trident cross-section within the spectrometer acceptance and a mass window of width δm by [8]

$$\frac{d\sigma(e^-Z \to e^-Z(A' \to \ell^+\ell^-))}{d\sigma(e^-Z \to e^-Z(\gamma^* \to \ell^+\ell^-))} = \left(\frac{3\pi\epsilon^2}{2N_{\rm eff}\alpha}\right)\left(\frac{m_{A'}}{\delta m}\right), \tag{18}$$

where $N_{\rm eff}$ counts the number of available decay products and is defined below equation (15). This exact analytic formula was also checked with a MC simulation of both the A' signal and the radiative tridents background restricted to a small mass window δm, and we find nearly perfect agreement. Thus, the radiative subsample can be used to analyze the signal, which simplifies the analysis considerably.

It is instructive to compare kinematic features of the radiative and Bethe-Heitler distributions, as the most sensitive experiment maximizes acceptance of radiative events and rejection of Bethe-Heitler tridents. Although the Bethe-Heitler process has a much larger total cross-sections than either the signal or the radiative trident background, it can be significantly reduced by exploiting its very different kinematics. In particular, the A' carries most of the beam energy (see discussion in §3), while the recoiling electron is very soft and scatters to a wide angle. In contrast, the Bethe-Heitler process is not enhanced at high pair energies. Moreover, Bethe-Heitler processes have a forward singularity that strongly favors asymmetric configurations with one energetic, forward electron or positron and the other constituent of the pair much softer.

These properties are discussed further in the Appendix of [8], and illustrated in Figure 13, which shows a scatterplot of the energy of the positron and the higher-energy electron for the signal (red crosses) and Bethe-Heitler background (black dots). The signal electron-positron pairs are clearly concentrated near the kinematic limit, $E(e^+) + E(e^-) \approx E_{beam}$. Background rejection is optimized in symmetric configurations with equal angles for the two

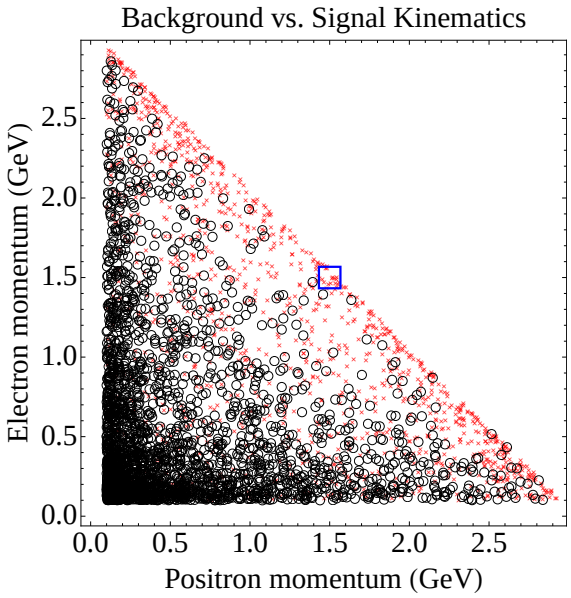

Figure 13: Positron and electron momenta in A' signal events with $m_{A'} = 200$ MeV (red crosses) and in Bethe-Heitler background events, for a 3 GeV beam energy. Comparably sized signal and Bethe-Heitler samples were used to highlight the kinematics of both; in fact the expected signals are much weaker than the Bethe-Heitler process. The clustering of A' events at high momenta near the kinematic limit and of Bethe-Heitler events along both axes are evident. A spectrometer acceptance window that optimizes signal sensitivity is indicated by the blue box.

spectrometers and momentum acceptance of each spectrometer close to half the beam energy (blue box).

While the signal over background (S/B) can be significantly improved with a judicious choice of kinematic cuts, the final S/B in a small resolution limited mass window is still very low, $\sim 1\%$. A "bump-hunt" for a small signal peak over the continuous background needs to be performed. This requires an excellent mass resolution, which has an important impact on target design and calls for a target that is tilted with respect to the beam line (see Appendix B for a discussion of the mass resolution).

5.1 Calculation of the ϵ reach

For all cross sections and rates of reactions described in this proposal, Monte Carlo based calculations were performed over a grid of beam energy settings and central spectrometer angular settings. Interpolation was used to extend this grid continuously to intermediate beam energies and angles — all rates exhibited expected power law behavior, thereby providing confidence in the reliability of an interpolation. Additional cross checks at specific points were performed to test the accuracy of our interpolation, which was generally better than $\sim 5\%$.

In order to calculate the α'/α reach of the proposed experiment for a particular choice of target nucleus, spectrometer angular setting, profile of wire mesh target, and momentum bite, the following procedure is performed:

- Monte Carlo events are simulated for the Bethe-Heitler, radiative tridents, and the continuum trident background including the full interference effects between the diagrams. The latter background is computationally intensive, and only a small statistics sample is generated, sufficient to obtain the cross-section from MadEvent.
- The cross-section ratio of the full continuum background (with interference effects) to the sum of the Bethe-Heitler and radiative tridents is calculated, and represents a multiplicative factor by which the latter must be multiplied to get the background cross-section.
- The rates of all reactions impinging the spectrometer acceptance were calculated by integrating over a chosen target profile, which usually extended from 4.5 to 5.5 degrees. For Bethe-Heitler, radiative tridents, and the continuum trident background, the calculation of the rate was performed as a function of invariant mass.
- Using the expressions in Appendix B, we calculated the mass resolution δ_m. We then tiled the acceptance region with bins of size $2.5 \times \delta_m$ in invariant mass.
- As a function of α'/α, the total number of signal (S) and background (B) events was calculated with the help of (18) for each bin.
- We then set $S/\sqrt{B} = 2$, and solved for α'/α.

This procedure was used to calculate the reach in the α'/α and $m_{A'}$ parameter space shown in §8.

6 Backgrounds

In this section, we present an analysis of the backgrounds in the data. Table 2 summarizes the expected singles rates, trigger rates, and coincidence rates. The remainder of this section elaborates on these rates, and related physics considerations.

We present calculations of the electron, pion, and positron singles rates in §6.1. These rates were checked against measurements made by experiment E03-012 for a 5 GeV electron beam incident on a hydrogen target, with at 6° 2-GeV HRS setting. The final values of the electron and pion rates were obtained by means of the "Wiser" code [56]; positron singles rates from trident reactions were calculated using MadGraph and MadEvent [55], described in §5. The considerations of §6.2 determine trigger rates and upper bound on offline accidental rates shown in Table 2.

Besides the trident events discussed in §5, an additional source of true coincidence events is the "two-step" (incoherent) trident process, in which an electron radiates a real, hard photon in the target that subsequently converts to a high-mass e^+e^- pair. We discuss a calculation of this rate in §6.3. For thin targets, it is suppressed compared to the trident rate, and so it is sub-dominant for all the settings we consider.

6.1 Inclusive rates

There are three main contributions to the counting rate in the spectrometers at small angles. They are due to electrons, pions, and protons scattered into the HRS acceptance. We discuss

Settings	**A**	**B**	**C**	**D**
Beam energy (GeV)	2.302	4.482	1.1	3.3
Central angle	5.0°	5.5°	5.0°	5.0°
Effective angles	(4.5,5.5)	(5.25,6.0)	(4.5,5.5)	(4.5,5.5)
Target T/X_0 (ratio[a])	4.25% (1:1)	10% (1:1)	0.58% (1:3)	10% (1:1)
Beam current (μA)	80	80	80	80
Central momentum (GeV)	1.145	2.230	0.545	1.634
Singles (negative polarity)				
e^- (MHz)	4.5	0.7	6.	2.9
π^- (MHz)	0.64	2.20	0.036	2.50
Singles (positive polarity)				
$\pi+$ [p] (kHz)	640.	2200	36.	2500.
e^+: QED (kHz)	31.	3.6	24.	23.
e^+: π^0 decay (kHz)	2	7	0.03	9
Total e^+ (kHz)	33.	10.6	24.03	32.
Trigger/DAQ				
Accidental trigger[b] (kHz)	3.55	0.47	2.93	3.33
True coinc. trigger (kHz)	0.65	0.09	0.36	0.6
Total trigger (kHz)	4.20	0.56	3.29	3.93
Offline Signal & Background Rates				
Trident (Hz)	610	70	350	530
Two-step (Hz)	35	15	5	75
Accidental Background[c] (Hz)	74	3.8	72	47

[a] The listed total target thickness is split between two sets of wire mesh planes, located at different z to produce the two indicated effective angles. The numbers in parentheses denote the ratio of target thickness at the larger effective angle to that at the smaller effective angle.

[b] Trigger: Coincidence with 20 ns time window between S0-N (assuming pions are rejected by a factor of 100) and S0-P signals.

[c] Dominated by e^+e^- accidental rate. We assume pion rejection by a factor of 10^4 in offline cuts, a 2 ns time window and additional factor of 4 rejection of accidentals from the target vertex. Further rejection using kinematics is expected, but not included in the table.

Table 2: Expected counting rates for proposed experiment. Settings A and B comprise the primary run plan, while settings C and D are additional possible settings at intermediate energies that may be possible in early running.

electron, pion, and proton singles rates below. The positron singles rates are dominated by trident events in which only the positron enters spectrometer acceptance. These rates have been calculated for each spectrometer setting using the same techniques as for pair production, discussed in §5.

6.1.1 The electron singles rates in HRS

The three contributions to the electron rate in the HRS at the proposed momentum settings are:

- Inelastic scattering
- Radiative elastic electron-nuclei scattering
- Radiative quasi-elastic electron-nucleon scattering.

The differential cross section of inelastic eN scattering processes is written in the standard notation as

$$\frac{d^2\sigma}{dE'd\Omega_{e'}} = \frac{\alpha^2}{4E^2\sin^4(\frac{\theta}{2})}\left[W_2(q^2,\nu)\cos^2\left(\frac{\theta}{2}\right) + 2W_1(q^2,\nu)\sin^2\left(\frac{\theta}{2}\right)\right]. \tag{19}$$

For E, $E' \gg M_{_N}$ and finite q^2, ν, we will use

$$\frac{d^2\sigma}{dE'd\Omega_{e'}} \approx \frac{\alpha^2}{4E^2\sin^4(\frac{\theta}{2})}\frac{F_2(q^2,\nu)}{\nu}. \tag{20}$$

For the elastic and quasi-elastic processes with low momentum transfer and very small scattering angle only the contribution from Coulomb scattering is important. The radiative elastic scattering cross section can be estimated as

$$\begin{aligned}\tfrac{d^2\sigma}{dE'd\Omega_{e'}} &\approx \tfrac{\alpha^2}{4(E')^2\sin^4(\frac{\theta}{2})}\times \\ \{Z^2\cdot F^2(E'\theta)\times\Big[(\tfrac{\alpha}{\pi}\ln(\tfrac{E'\theta}{m_e})^2 + t_{eff})/(E-E')\Big]\times\big[1+(\tfrac{E'}{E})^2\cdot F^2(E\theta)/F^2(E'\theta)\big] + \\ Z\times\Big[(\tfrac{\alpha}{\pi}\ln(\tfrac{E'\theta}{m_e})^2 + t_{eff})/(E-E')\Big]\times\big[1+(\tfrac{E'}{E})^2\big]\},\end{aligned}$$

where $F(E'\theta)$ is the nuclei elastic form factor at three-momentum transfer equal to $E'\theta$ and t_{eff} is the effective target thickness in units of radiation length. The effective target thickness t_{eff} has two parts. The first one is a probability of an internal radiation before scattering $\frac{\alpha}{\pi}\ln(E'\theta/m_e)^2$. The second accounts for the probability of an external radiation before scattering, which is about half of the target thickness. The form factor of the tungsten nucleus for very low values of q can be estimated from its radius $R \approx 7$ fm as $(1-(qR)^2/6)$ and for sufficiently high q from a Fourier transform of the density approximated by a step function. The radiation after scattering taken is taken into account by the term proportional to $(\frac{E'}{E})^2$.

6.1.2 The pion singles rates in the HRS

The differential cross section for the electro-production of pions can be written as

$$\frac{d^3\sigma}{dE'd\Omega_{e'}d\Omega_\pi} = \Gamma \cdot \frac{d\sigma_{\gamma^*,\pi}}{d\Omega_\pi}, \tag{21}$$

where Γ is the virtual photon flux factor given by

$$\Gamma = \frac{\alpha}{2\pi^2}\frac{E'}{E}\frac{s-M^2}{2MQ^2}\frac{1}{1-\epsilon}, \tag{22}$$

and $\frac{d\sigma_{\gamma^*,\pi}}{d\Omega_\pi}$ is the cross section for pion production by the virtual photon. Integration over the electron scattering angle leads to an estimate of $\Gamma \approx 0.015$, see Figure 14. At small

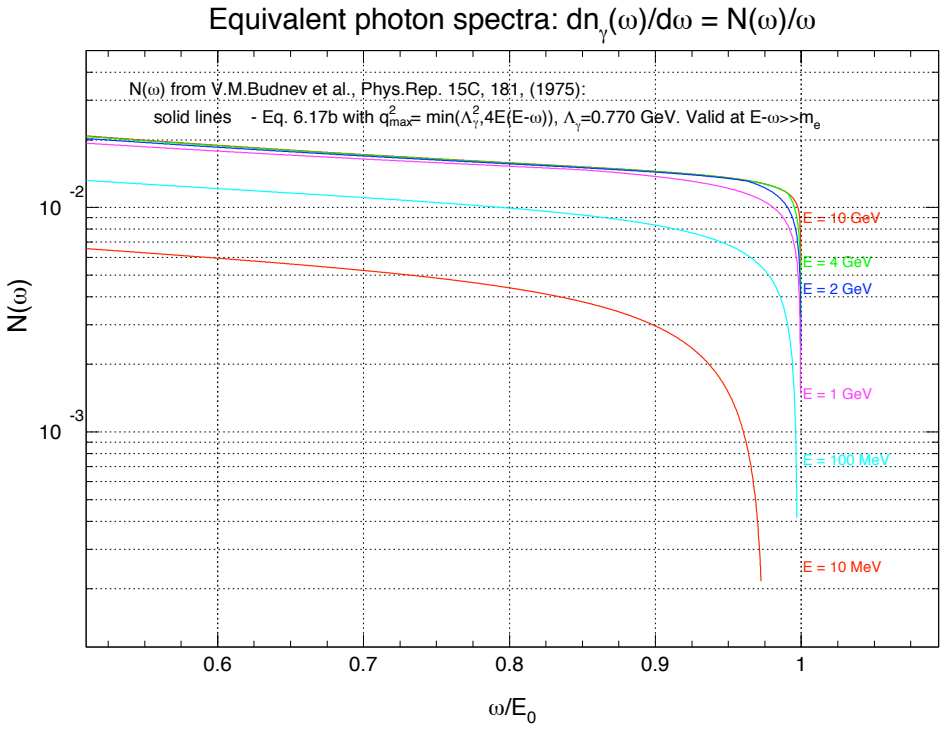

Figure 14: The photon flux factor according to the effective photon approximation [57].

scattering angles, where $Q^2 \ll \nu^2$, only transverse terms of the cross section contribute. Our calculations of the cross-section were performed using the "EPC" code [58] with a normalization factor of 1.5 obtained from our measurements of a 5 GeV electron beam on a hydrogen target with the HRSs at 6° and 2 GeV/c settings [59]. At these kinematics, the prediction of the Wiser code [56] is in very good agreement with our experimental data.

Table 1
$E\,d^3\sigma/d^3p$ [μb/GeV^2] at E_γ = 3.2 GeV, θ_{lab} = 2°

x_π	π^+	π^-	x_p	p	x_K	K^+
0.994	15.1 ± 0.41	–	0.854	2.94 ± 0.23	–	–
0.900	32.3 ± 0.76	49.7 ± 1.0	0.746	4.75 ± 0.34	0.977	4.05 ± 0.23
0.838	48.9 ± 1.4	77.5 ± 1.8	0.673	6.81 ± 0.58	0.902	4.49 ± 0.52
0.806	54.5 ± 1.5	67.2 ± 1.6	0.635	8.10 ± 0.54	0.865	3.35 ± 0.47
0.775	61.6 ± 1.9	56.4 ± 2.7	0.598	9.26 ± 0.70	0.827	4.07 ± 0.62
0.712	72.9 ± 2.6	57.7 ± 2.9	0.521	13.0 ± 1.1	0.751	3.05 ± 0.64
0.618	85.2 ± 5.0	64.0 ± 4.9	0.400	24.6 ± 2.6	–	–
0.524	76.9 ± 6.90	73.5 ± 5.7	0.272	33.7 ± 4.4	–	–
0.429	90.9 ± 9.53	68.7 ± 8.5	0.132	54.3 ± 7.2	–	–
0.381	84.3 ± 9.94	92.0 ± 8.6	0.056	54.7 ± 8.7	–	–
0.333	102.0 ± 11.60	80.0 ± 10.0	0.026	61.9 ± 12.8	–	–

Figure 15: The hadron production cross section from [60].

6.1.3 The proton singles rates in HRS

There were several measurements of the inclusive hadron yield in the reaction $H(\gamma, h)X$ at energies of several GeV, see e.g. [60, 61, 62]. In addition, there is a recent measurement of the electro-production by a 5 GeV beam [59]. There are three computer codes, which allow us to calculate the hadron production cross section: the so-called Wiser code [56], the EPC code [58], and the DINREG event generator in GEANT [63].

The overall result is that the proton yield at the proposed kinematics will be about 4 to 6 times lower than the pion yield, as illustrated in the table in Figure 15. Here the Feynman variable is $x = p^h_{\parallel,cm}/p^h_{max,cm}$. For example, for $E_{beam} = 3.2$ GeV, $\theta = 5°$ the particle momentum 1.6 GeV/c corresponds to the $x_\pi = 0.50$ and the $x_p = 0.48$. The resulting yield ratio of protons to pions is 1.0/5.5 before correcting for the pion decay, or 1.0/4.2 at the focal plane.

6.2 True and accidental coincidences

The accidental coincidences between the electron and the positron arms will be a dominant part of the recorded events. A typical composition of the single rate in the spectrometers is expected to be $e^-/\pi^- \approx 80/20$ in the negative polarity arm and $\pi^+/p/e^+ \approx 80/19/1$ in the positive polarity arm. The fraction of the true coincidence events could be up to 50% for the $e^-\pi^+$ rate within a 2 ns time window, and could be significant for the e^-p events in certain regions of momenta — see an example of the relative time distribution between the signals of two arms in Figure 16. Selection of the true coincidence events, which are mostly $e^-\pi^+$, within a 2 ns time window allows us to calibrate the detector timing offsets, using production data, and optimize the tracking analysis.

The true coincidence e^+e^- events will be selected by:

- The 2-ns coincidence time window;
- The 5-cm target vertex correlation between arms;

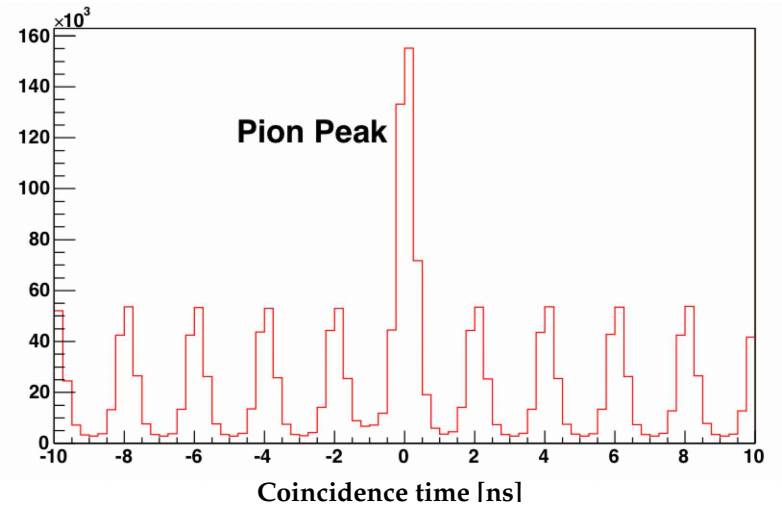

Figure 16: The event distribution over relative time between signals of two arms.

- Gas Cherenkov & shower calorimeter identification in both arms.

The ratio of the signal (electroproduction of e^+e^- pair dues to QED) to the background (accidental e^+e^- and true $e^-\pi^+$ events) is expected to be on the order of 10 to 1, which should not affect sensitivity for the search of the narrow resonance.

6.3 Electron-Positron Pairs from Two-Step Tridents

We have already discussed the principal source of electron-positron pairs, namely the trident process, in §5. An additional reaction that gives rise to high-energy electron-positron pairs is the "two-step" (or incoherent) trident process, consisting of radiation of a hard photon in the front of the target, followed by the conversion of this photon to a high-mass pair further along the target. The rate for this process evidently goes as T^2, and it can be $\mathcal{O}(1)$ for $T \sim 0.1$.

At a point t radiation lengths into the target, the intensity of photons carrying a fraction $x = E/E_0$ of the beam energy is approximately [64]

$$I_\gamma(t,x) \approx \frac{1}{x}\frac{(1-x)^{4t/3} - e^{-7t/9}}{\frac{7}{9} + 43\log(1-x)}. \tag{23}$$

The photoproduction process was then simulated to determine the pair rate within spectrometer acceptance, in the case of photons carrying the entire beam energy ($x = 1$). For spectrometer windows centered near $p = E_0/2$, the spectrometer acceptance grows linearly from $x_{min} = 2p_{min}/E_0$ to $x = 1$, and vanishes below x_{min}. In this approximation, we have integrated (23) over x and over the thickness of the target to obtain the numbers in Table 2. Even for the thickest targets considered, two-step trident events represent only a 30% correction to the total e^+e^- pair rate. We have also computed the contribution of two-step tridents to the positron singles rate, which is negligible.

7 Experiment

In this section, we will present a description of the experimental concept and the operation of the spectrometer(s) detector system. We will also address the calibration of the spectrometer optics and the acceptance variation systematics.

7.1 Concept of the experiment

The experiment will measure the invariant mass spectrum of e^+e^- pairs produced by an incident beam of electrons on a tungsten target. The search for an A' peak will be done in the mass range from $\sim$ 65 MeV to 550 MeV. The experiment will be performed in Hall A at JLab using two high-resolution spectrometers [54] together with a septa magnet constructed for the PREX experiment [2]. The electron beam with a current of 80 μA will be incident on a solid target located on a standard target ladder in a standard scattering chamber. The target will be made of tungsten wires strung together in a horizontal plane orthogonal to the beam direction. The target plane will be mounted at an angle of about 10 mrad with respect to the horizontal plane. The beam will be rastered by $\pm$0.25 mm in the horizontal and $\pm$2.5 mm in the vertical direction.

The electron will be detected in the HRS-R and the positron will be detected in the HRS-L. The trigger will be formed by a coincidence of two signals from the S0 counters of the two arms and a coincidence of the signal in the S0 counters with a signal from the Gas Cherenkov counter of the HRS-L (positive polarity arm). A timing window of 20 ns will be used for the first coincdence and 40 ns for the second coincidence. The resulting signal will be used as a primary trigger of DAQ.

An additional logic will be arranged with a 100 ns wide coincidence window between signals from the S0 counters. This second type of trigger will be prescaled by a factor 20 for DAQ.

7.2 Measurement of the particle track

There are two 2-m long vertical drift chambers (VDC) in the HRS detector package. These are used for the measurement of the track's coordinates and its direction in the focal plane. Each chamber has 368 wires in each "U" and "V" direction. The chamber provides coordinate resolution of at least 0.2 mm. The average number of wires per track is 4–5 depending on the track angle with respect to the chamber plane. The distance of 500 mm between the chambers allows determination of the track direction with angular resolution of 0.5 mrad. The chambers are instrumented with the LeCroy 2735 amplifier/discriminator cards and the LeCroy 1877 multi-hit FASTBUS TDC.

7.3 Identification of electrons and positrons

The HRS spectrometer detector packages are equipped with Gas Cherenkov counters and two-layer lead-glass calorimeters for identification of electrons and positrons. The Gas Cherenkov counter has ten PMTs and will be used for online PID with a timing window of 40 ns. The online rejection factor is about 100 (not including the accidental coincidences). The combined pion rejection factor (Gas Cherenkov's and Calorimeter's) in the offline analysis is at least as high as 10,000.

7.4 Smoothness of the invariant mass acceptance

The experiment will search for a narrow peak in the invariant mass spectrum of e^+e^- pairs, whose resolution should be as high as possible and at least much better than the width of the acceptance. Because a high level of statistical precision is needed, it is especially important to have a very small level of systematics in the proposed experiment. The systematics arise from variations in the acceptance and detection efficiency.

The pair invariant mass is $m_\pm^2 \approx 2m_e^2 + p_+ \cdot p_- \cdot [(\theta_+ + \theta_-)^2 - \theta_+\theta_-\phi^2]$, where p_+, p_- are the positron and the electron momenta, the θ_+, θ_- are the scattering angles, and the ϕ is an angle between the scattering planes. The efficiency for a given value of $m_\pm$ is defined by an integral over all the phase space of the detector system. The most important part of this integral is over p_+, p_-, θ_+, and θ_-. The range of the momentum for one of the particles in the pair (p_+ or p_-) each leads to about 10% variation in $m_\pm^2$. The range for the scattering angles (θ_+ or θ_-) each leads to about 25% variation of $m_\pm^2$. Let us assume that the detector efficiency has a dip by 10% within a positron momentum window of width $dp \sim 1\%$. Fixing the other variables (p_-, θ_+, θ_-), the invariant mass spectra will also have a 10% dip with a 1% width. When integrated over three other variables, however, the dip will be spread over a full range of masses, and the local size of the dip will be reduced by a factor of $10 \times (25)^2 = 6250$, so the 10% dip becomes a 0.0016% step. Such a level of systematics is very small because it corresponds to statistics of 4×10^9 events within a 1% mass interval (compared to the 10^7 relevant statistics in the proposed experiment).

Figure 17 shows the experimental distribution for $m_{e^+e^-}$ with small statistics available from E04-012 experiment. The acceptance has a smooth shape with about 25% FWHM. According to the run plan the data will be collected at several overlapping settings and result in a relatively smooth spectrum from ~ 65 MeV up to 550 MeV.

8 Proposed measurements

We propose a twelve-day run in the configuration "B" of Table 3 (see also Table 2) and six-day runs in each of the remaining configurations, to search for new resonances in e^+e^- trident spectra from 65 to 550 MeV. Settings "A" and "B" are the primary run plan, using nominal beam energies for 12 GeV running. The settings "C" and "D" correspond to additional configurations that may be allowed in early running. For settings "A" and "C", the target thickness and beam current have been optimized to accumulate the largest possible sample of trident events without saturating the data acquisition system. Settings "B" and "D" are far from data acquisition limits, but we do not use $T/X_0 > 10\%$ to avoid limits on the total radiation produced.

The mass range from 65 to 550 MeV is chosen to take advantage of the Hall A HRS spectrometers, as well as for its theoretical interest. Lower masses are more effectively probed by vertexing experiments. Settings at higher masses are possible but have significantly reduced sensitivity and are better suited to exploration with higher-acceptance equipment and an experiment optimized to accept muon and pion pairs as well as electrons.

As illustrated in Figure 18, the sensitivity of the experiment is greatly enhanced by including the intermediate-energy settings "C" and "D". At beam energy E, a spectrometer setting with opening angle θ and momentum acceptance near $E/2$ is sensitive to A' masses $\approx \theta E$. Each spectrometer setting is sensitive to A' resonances 15% higher or lower than the

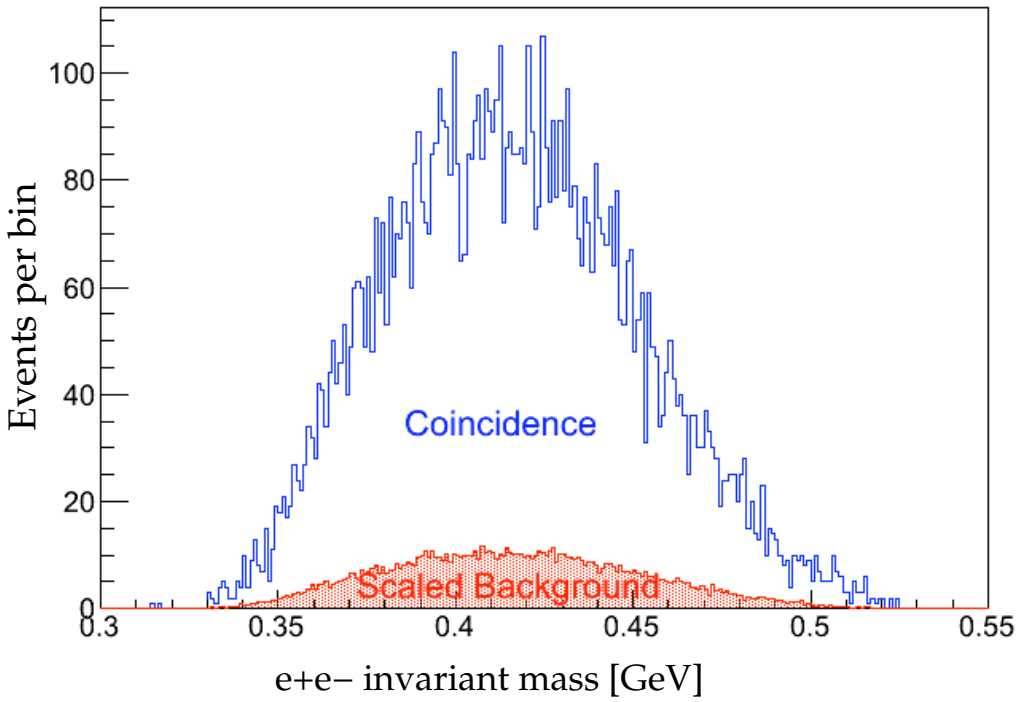

Figure 17: The invariant mass distribution (in GeV) for e_+e_- events in the E04-012 experiment [59]. The red curve shows the accidental background distribution obtained with a wider time window and scaled to the 2 ns time window.

optimal mass, for fixed central angle. This range is extended to ±30% in mass, shown in Figure 18, by using a long target. The mass range from 120 to 550 MeV could be covered (with reduced sensitivity) using only the 2.302 and 4.482 GeV beam energy settings, but using multiple nominal central angles.

In each setting, the proposed experiment will accumulate between 70 and 300 million trident events. With these statistics, it will be possible to search offline for small resonances comprising a few thousandths of the collected data in a resolution-limited window. This will allow sensitivity to new gauge boson couplings α'/α as low as 10^{-7} over the broad mass range of the experiment, as summarized in Figure 18. This sensitivity would improve on the cross-section limits from past experiments by a factor of $\sim 10 - 1000$.

As a specific example, we have illustrated the expected sensitivity of setting A to A' signals with different ϵ in Figure 19. Each component of the target populates a different invariant mass distribution; for simplicity we consider only the contribution from the front planes of the target, with $\theta_{eff} \approx 5.5°$. The left panel illustrates the absolute size of A' signals at $m_{A'} = 200$ MeV compared to the continuum trident background (gray line) and the size of 2 and 5-sigma statistical fluctuations (blue and green dashed lines), while the right panel illustrates how the same signals would appear after subtracting a smooth parameterization of the background. The purple curves in each panel corresponds to an A' signal with $\alpha'/\alpha = 7 \times 10^{-6}$ at 200 MeV, which according to the estimates in §2.4 would not be seen or excluded at 2σ by a future KLOE search in $\phi \to \eta A'$. The red curve has $\alpha'/\alpha = 1.3 \times 10^{-7}$, corresponding to the

Settings	**A**	**B**	**C**	**D**
Beam energy (GeV)	2.302	4.482	1.1	3.3
Beam current (μA)	80	80	80	80
Nominal central angle	5.0°	5.5°	5.0°	5.0°
Time Requested (hrs)				
Energy change	–	4	4	4
Angle change	–	16	–	–
Magnet setup	4	4	4	4
Optics calibration	4	4	4	4
10% $\mathcal{L}$	2	2	2	2
Normal $\mathcal{L}$	144	288	144	144
Total	154	318	158	158

Table 3: Run plan for the proposed experiment. Settings A and B comprise the primary run plan, while C and D are possible additional settings if flexible beam energies are permitted in early running.

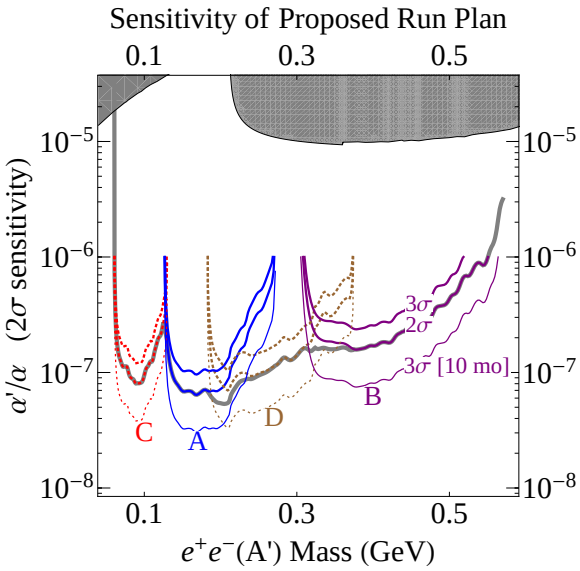

Figure 18: Expected 2σ exclusion sensitivity for ϵ for the run plan outlined in Table 3. Settings A and B comprise the primary run plan, while C and D are possible additional settings if flexible beam energies are permitted in early running, which considerably increase the range of masses over which the proposed experiment is sensitive. Existing constraints are shown in the gray shaded regions. The colored curves correspond to the sensitivity in each of the individual energy settings, and the thick gray curve reflects the sensitivity of a combined analysis. 3.

expected "5σ" sensitivity (not accounting for the trials factor) in the proposed experiment.

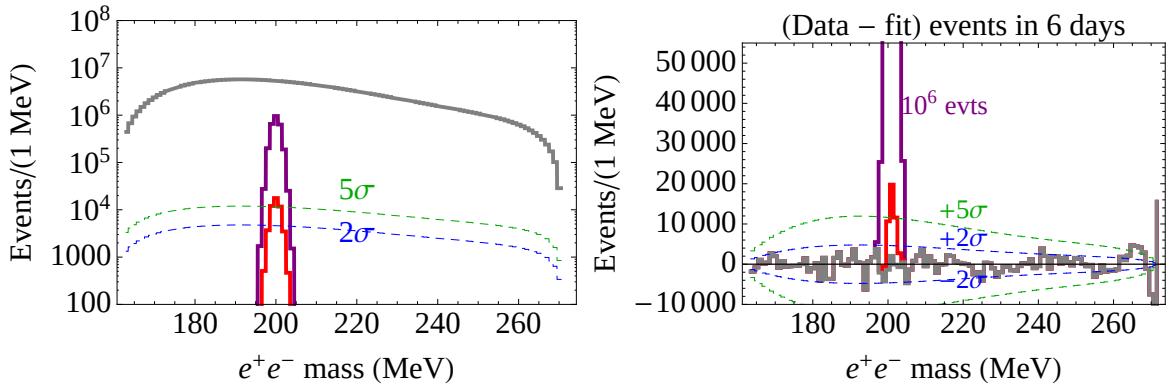

Figure 19: Comparison of signal rates in six days of running at setting A to expected background and statistical sensitivity. **Left Figure:** The resonances in purple and red lines correspond to A' signals at 200 MeV, smeared by a Gaussian to model detector resolution and multiple scattering, with $\alpha'/\alpha = 6.5 \times 10^{-6}$ and 1.3×10^{-7}, respectively. The upper (purple) signal is just beyond the 2σ expected sensitivity of a KLOE analysis, while the lower (red) signal corresponds to the "5σ" sensitivity (not including a trials factor) of this experiment. The gray line is the simulated invariant mass distribution for the continuum trident background, and the blue and green dashed lines reflect the size of 2 and 5σ Poisson fluctuations. **Right Figure:** The gray line corresponds to the bin-by-bin differences between pseudodata containing no signal and a smooth fit to this pseudodata. Analogous subtractions when a signal is present are shown in purple and red, with the same ϵ as in the left figure. Again the blue and green dashed lines reflect the size of 2 and 5σ Poisson fluctuations.

8.1 Beam time request

The beam time request for the proposed experiment is summarized in Table 4.

9 Technical considerations

9.1 The target

A high-Z target provides the best signal to noise for the proposed experiment. The thickness of the target is always a compromise between the momentum and angular resolution versus the counting rate. The proposed experiment requires a very good resolution for the invariant mass of the produced electron-positron pair in contrast to many other HRS experiments which had to measure the missing mass. As a result, the thickness of material in the path of the beam electrons does not affect the experimental resolution, and only the scattering of the outgoing pair components needs to be minimized.

The specific design of the target should take into account heat load by the beam. This is, as usual, mitigated by rastering the beam and using materials like tantalum or tungsten. For minimization of the amount of material in the path of the outgoing electron-positron pair, t_{pair}, we propose a tilted target (see Figure 6). This target could be made of a thin

Settings	**A**	**B**	**C**	**D**
Beam energy (GeV)	2.302	4.482	1.1	3.3
Beam current (μA)	80	80	80	80
Target thickness (X_0)	4.25%	10%	0.58%	10%
Beam on target (hrs)	146	290	146	146
Time Requested (hrs)	154	318	158	158
	→ 788 (∼33 days total)			

Table 4: Beam time request for the proposed experiment. Settings A and B comprise the primary run plan, while C and D are possible additional settings if flexible beam energies are permitted in early running. Including these settings would increase by a factor of two the mass range of maximal sensitivity, as illustrated by the curves in Fig. 18.

foil, the plane of which is almost parallel to the beam direction. However, we choose to use a wire mesh plane of closely spaced tungsten wires. Each wire has a diameter of $10\mu m$, with a spacing that can vary from 150μm to 0.5 mm. The wires are sufficiently spaced so that outgoing electron-positron pairs only traverse a single wire. Beam electrons on the other hand can pass through up to 7, because the wire mesh plane is tilted at 10 mrad.

The tilted target cools from a large area; for example, with the raster size 0.5×5 mm and proposed geometry (Figure 6), the cooling area is 20 cm^2. For the parameters of the proposed experiment (electron beam of 80 μA on 10% X0 tungsten target) the head load is about 140 W (or 7 W/cm^2), which results in the equilibrium target temperature of 1000°K. Experimental study has demonstrated that 1 kW/cm^2 is a safe level for a tungsten foil target [65], so we expect that the wire mesh target will perform quite well.

The minimum length of the target is 100 mm, so 4-5 planes can be used (see Figure 6). We are expecting that for the angle between the target plane and the beam direction on the level of 10 mrad, the beam-target geometry will be stable; however, further reduction of this angle could lead to a problem in practice due to known mechanical properties of the target mechanism and reproducibility of the target position. The practical limit on the target design is also defined by the acceptable length of the target which should fit the the scattering chamber (100 cm) and material thickness. Available from stock are tungsten foils of thickness 20 μm, which is about 10 times larger than required. As mentioned, it is preferable to use a set of of strung wires, and in this case diameters as small as 4 μm are possible. By adjusting wire spacing, the effective thickness can be reduced to a fraction of a micron.

9.2 The septum magnet

A new room-temperature septum magnet has been designed by Paul Brindza and Al Gavalya at JLab for the PREX experiment [2]. The nominal scattering angle is 5° and the energy is 1.05 GeV. The magnet will be reconfigured for the 2 GeV momentum setting. It was demonstrated in a recent hyper-nuclei experiment with another septum magnet [66] that the vacuum coupling allows us to reach very high momentum and angular resolutions.

9.3 Electronics and trigger

We presented the main trigger in §4.5, and repeat it here for convenience. The main trigger for this experiment is given by a coincidence between signals from the two arms. The coincidence will be formed by two independent logic schemes, one with a timing window of 20 ns between the signals of the S0 scintillator counters (S0-Negative and S0-Positive) and a 40 ns time interval between the scintillator counter signals and the Gas Cherenkov counter of the positron arm, and a second with a timing window of 100 ns. The second signal will be prescaled by a factor 20. Most of the DAQ rate will come from events with a coincident electron and positron within a 20 ns time interval. We will in addition have several auxiliary triggers to monitor the equipment.

See Table 2 for the expected rates.

9.4 The high rate operation of the VDC

The operation of the HRS tracking at a total rate higher than 100 kHz is not very common. However, the track rate of 30-50 kHz of elastic scattering events from a ^{12}C target was used during many HRS optics calibrations and provides a good test case. The rate of elastic events corresponds to the track density of about 10 kHz per cm of the chamber length. The length of the focal plane and the chamber is about 2 m. This means that the resolution is not affected at the rate of 2 MHz for the whole chamber at standard operational voltage. During the recent BigBite experiment, the MWDC operated with a high detection efficiency with a hit rate of 20 MHz or 100 kHz per wire. The operation at such high rates required the development of custom-made electronics, which reduce the signal from the wire by a factor of 5. This electronics is available and could be installed in the HRS in a few days. Reduction of the required signal amplitude by a factor of 5 means that in each hit there will be 5 times fewer ions. The reduction of the ion cloud charge directly translates to an additional factor of 5 in rate capability, which brings the VDC limit to at least 10 MHz for the whole chamber. The development of a new A/D card based on the MAD chip was presented in our contribution to the 2007 Hall A annual report [67].

In most experiments with the HRS, the tracking rate in the VDC is very low compared with the projected rate for this experiment. However, in several measurements, such as the pentaquark search E04-012 and a number of hypernuclei experiments performed with the septum magnet, the rate was 250-300 kHz. Analysis of that data did not encounter problems because the probability of multiple tracks was just 10%, and it is well understood how to correct for these events. We present here considerations for the analysis, which justify our plan to use the VDC at a maximum of 5-6 MHz track rate.

The probability of losing a track can be estimated as follows: The VDC has a maximum drift time of 350 ns, which corresponds to 1.75 accidental tracks per event at 5 MHz. The drift time recorded for the wires of the accidental track will have a mismatch relative to the trigger time, which allows such tracks to be rejected. The rejection factor is defined by the ratio of the width of the mismatch time distribution, about 300-500 ns, to the width of the time window required for full efficiency of the real coincidence tracks, which is about 25 ns. Figure 20 illustrates the location of the track ions from the correct track and the shifted accidental "track", with the latter having mismatched timing. The rejection of accidental tracks will be done for individual U and V planes before reconstruction of the X/Y coordinate. The rejection factor of 10 reduces the number of accidental tracks from 1.75 per event to

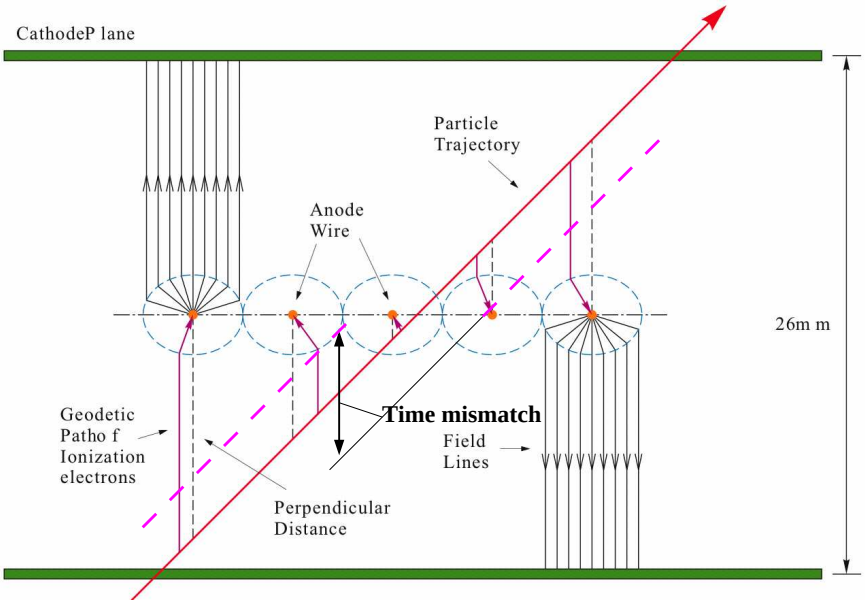

Figure 20: The illustration of the VDC drift pattern. The real track (the solid red line) has a well matched "time" between the "upper" and the "lower" times. The accidental track (the dashed violet line) has a large mismatch.

0.2 per event. Because this rejection factor is independent for two VDC chambers, the probability of an accidental track being reconstructed in both VDCs (four planes) will be at most 0.05. In these remaining 5% events, the real track will be determined using the fact that its trajectory intersects the proper scintillator paddle of the high resolution plane that is segmented into 16 paddles. As a result, the probability of a false track drops below 0.005.

For an average event, the wire multiplicity is 4.5, so the probability of having two tracks inside one group (5 wires) is less than 3%. Such events will most likely be rejected and lead to only a small tracking inefficiency.

10 Conclusion

We request 33 days (30 days of beam) to measure the electron-positron pair mass spectrum and search for new gauge bosons A' in the mass range 65 MeV $< m_{A'} <$ 550 MeV that have weak coupling to the electron. Parametrizing this coupling by the ratio α'/α that controls the A' production cross-section, this experiment would probe α'/α as small as $\sim (6-8) \times 10^{-8}$ at masses from 65 to 300 MeV, and $\alpha'/\alpha \sim (2-3) \times 10^{-7}$ at masses up to 525 MeV, making it sensitive to production rates 10–1000 times lower than the best current limits set by measurements of the anomalous muon magnetic moment and by direct searches at BaBar. The experiment uses the JLab electron beam in Hall A at energies of 1.1, 2.302, 3.3, and 4.482 GeV incident on a long (50 cm) thin tilted tungsten wire mesh target, and both arms of the High Resolution Spectrometer at angles between 5.0° and 5.5° relative to the nominal target position. The experiment can determine the mass of an A' to an accuracy of $\sim$ 1–2 MeV.

Constraints on new vector bosons with mass near 50 MeV – 1 GeV are remarkably weak. However, such light force carriers are well motivated theoretically, and several recent anomalies from terrestrial and satellite experiments suggest that dark matter interacting with Standard Model particles has interactions with new vector bosons in precisely this mass range. The proposed experiment can probe these hypothetical particles with a sensitivity that is un-rivaled by any existing or planned experiment.

A Effective Photon Flux, Target Nucleus and Beam-Energy Dependence

In this appendix we summarize the formulas used in Section 3 for the reduced effective photon flux $\tilde{\chi}$, and highlight its dependence on the A' mass, target nucleus, and beam energy. The effective photon flux χ is obtained as in [50, 51] by integrating electromagnetic form-factors over allowed photon virtualities:

For a general electric form factor $G_2(t)$,

$$\chi \equiv \int_{t_{min}}^{t_{max}} dt \frac{t - t_{min}}{t^2} G_2(t) \tag{24}$$

(the other form factor, $G_1(t)$, contributes only a negligible amount in all cases of interest). Since we are dominated by a coherent scattering with $G_2 \propto Z^2$, it is useful to define a reduced photon flux,

$$\tilde{\chi} \equiv \chi / Z^2. \tag{25}$$

The integral in (24) receives equal contributions at all t, and so is logarithmically sensitive to $t_{min} = (m_{A'}^2/2E_0)^2$ and $t_{max} = m_{A'}^2$.

For most energies in question, $G_2(t)$ is dominated by an elastic component

$$G_{2,el}(t) = \left(\frac{a^2 t}{1 + a^2 t}\right)^2 \left(\frac{1}{1 + t/d}\right)^2 Z^2, \tag{26}$$

where the first term parametrizes electron screening (the elastic atomic form factor) with $a = 111\, Z^{-1/3}/m_e$, and the second finite nuclear size (the elastic nuclear form factor) with $d = 0.164\ \mathrm{GeV}^2 A^{-2/3}$. We have multiplied together the simple parametrizations used for each in [50]. The logarithm from integrating (24) is large for $t_{min} < d$, which is true for most of the range of interest. However, for heavy A', the elastic contribution is suppressed and is comparable to an inelastic term,

$$G_{2,in}(t) = \left(\frac{a'^2 t}{1 + a'^2 t}\right)^2 \left(\frac{1 + \frac{t}{4m_p^2}(\mu_p^2 - 1)}{(1 + \frac{t}{0.71\ \mathrm{GeV}^2})^4}\right)^2 Z, \tag{27}$$

where the first term parametrizes the inelastic atomic form factor and the second the inelastic nuclear form factor, and where $a' = 773\, Z^{-2/3}/m_e$, m_p is the proton mass, and $\mu_p = 2.79$ [50]. This expression is valid when $t/4m_p^2$ is small, which is the case for $m_{A'}$ in the range of interest in this paper. At large t the form factors will deviate from these simple parameterizations but can be measured from data. One can show that the contribution from the other inelastic nuclear form factor $G_1(t)$ is negligible.

The resulting reduced form factor $\tilde{\chi}(m^2, E_0) = \chi/Z^2$ are plotted in the left panel of Figure 21 as a function of e^+e^- mass for various electron energies (1, 2, 3, and 4 GeV) incident on a Tungsten target. The relative efficiency of A' production in targets of different compositions but the same thickness in radiation lengths is given by the ratio

$$R(Z_1, Z_2) = \frac{X_0(Z_1)\chi(Z_1, t)/A(Z_1)}{X_0(Z_2)\chi(Z_2, t)/A(Z_2)}. \tag{28}$$

For example the ratio $R(Si, W)$ is shown in the right panel of Figure 21, again as a function of e^+e^- mass for beam energies between 1 and 4 GeV.

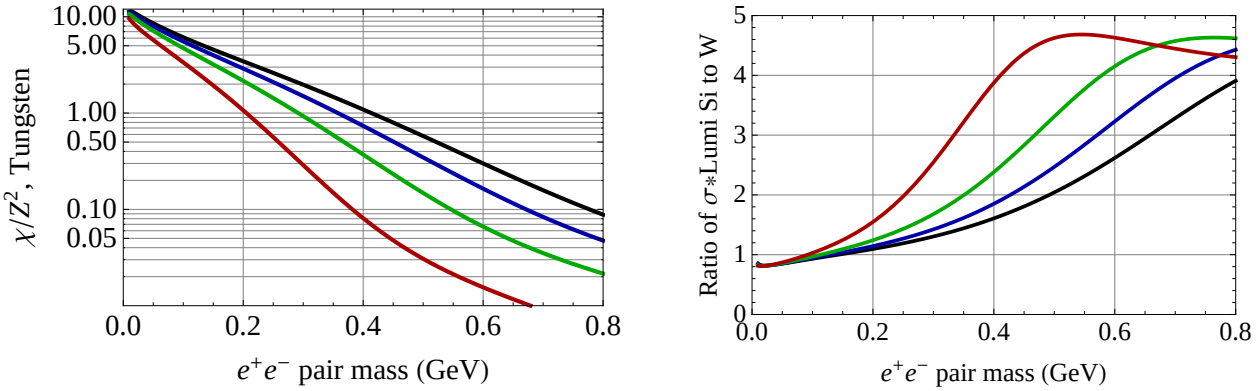

Figure 21: *Left:* The factor $\tilde{\chi} = \chi/Z^2$ defined in (25) and (24) as a function of e^+e^- mass for (bottom to top) 1, 2, 3, and 4 GeV incident electrons on a Tungsten target. *Right:* The ratio of (28) A' production rates per radiation length for Silicon and Tungsten targets, as a function of invariant mass and for beam energies (top to bottom at 0.4 GeV) 1, 2, 3, and 4 GeV incident electrons.

B Mass resolution

In this appendix, we briefly describe an estimate of the mass resolution of the spectrometer. Since we are looking for a small bump on the invariant mass spectrum distribution, an excellent mass resolution is essential to obtain a good reach in ϵ.

The mass resolution of the spectrometer, δ_m, is roughly given by

$$\left(\frac{\delta_m}{m}\right)^2 = \left(\frac{\delta_p}{p}\right)^2 + 0.5 \times \left(\frac{\delta_\theta}{\theta}\right)^2, \tag{29}$$

where δ_θ is the angular resolution of the electron or positron, and δ_p/p is the momentum resolution of the HRS, which is always less than 3×10^{-4} (in our estimates for the reach of ϵ, we take $\delta p/p$ to be equal to this upper bound). We have

$$(\delta_\theta)^2 = (\delta_{HRS})^2 + (\delta_\theta^{ms})^2, \tag{30}$$

where δ_{HRS} is the HRS angular resolution, which is ~ 0.5 mrad in the horizontal direction and ~ 1 mrad in the vertical direction. Moreover, δ_θ^{ms} represents the degradation of the resolution due to multiple Coulomb scattering in the target. It is given by the standard formula [53]

$$\delta_\theta^{ms} = \frac{13.6}{p[\text{MeV}]} \sqrt{\frac{t}{X_0}} \left[1 + 0.038 \ln\left(\frac{t}{X_0}\right)\right], \tag{31}$$

where t is the thickness in radiation lengths of the material along the path of the particle, X_0 is the radiation length of the target in g/cm^2, and p is the momentum of particle in MeV.

For the proposed experiment, the thickness of the target along the direction of the beam line varies from $t = 0.003X_0$ to $t = 0.09X_0$. However, in the case of a foil target or a target composed of several thin wires, the distance traversed by trident electron-positron pairs can be significantly smaller because the electron and positron have relatively large angles with respect to the beam line. For a foil, we can take $t \approx \frac{1}{2} t_f / \sin(\theta_p - \theta_f)$, where t_f is the

foil thickness and θ_f its angle relative to the beam line. In this case the effective thickness traversed by the beam is $T_0 = t_f / \sin\theta_f$.

In the case of a target composed of multiple wires, as was assumed in determining the experimental sensitivity, the wires can be spaced widely enough that the pair-produced particles need only travel through a single wire. In this case, t is typically the radius of the wire, which for Tungsten wire targets can be as small as 10μm, or $3 \times 10^{-3} X_0$. In this case, we find that the HRS angular resolution, δ_{HRS}, is comparable to the multiple scattering δ_θ^{ms} in the proposed experiment.

C Monte Carlo validation with E04-012 data

In this appendix, we briefly describe a validation of the Monte Carlo (MC) simulation of the signal, Bethe-Heitler and radiative trident backgrounds (shown in Figure 12 and discussed in §5), and the positron singles.

We first discuss a comparison of the MC with previous experimental results from the JLab experiment E04-012 [59]. This experiment consisted of a 5.01 GeV, $14.5\mu A$ electron beam incident on a 1.72% radiation length liquid Hydrogen target. The e^+ singles rate was measured to be ~ 1.1 kHz in a momentum window of $\pm 4\%$ around 1.93 GeV and an angular acceptance of 4.5 msr with an aspect ratio of 2-to-1 centered at an angle of 6°. The e^+e^- coincidence rate was measured at ~ 4 Hz for the same angular acceptance for both the electron and positron arm, and with a momentum window of $\pm 4\%$ around 1.93 GeV for the positron and $\pm 4\%$ around 1.98 GeV for the electron. We simulated this with MadGraph and MadEvent [55] as described in §5, using a form factor for Hydrogen given in [50]. We find a e^+ singles rate of ~ 965 Hz and an e^+e^- coincidence rate of 3.9 Hz, which agrees with the measured rates to within $\sim 19\%$ and a few percent, respectively.

We have also verified the implementation of form factors in Monte Carlo by simulating photo-production of electrons and muons off Tungsten and Beryllium with MadGraph and MadEvent. The resulting cross-sections agree to within 30% with published computations in the Weizsäcker-Williams approximation [51].

References

[1] B. Holdom, *Two U(1)'s and Epsilon Charge Shifts*, *Phys. Lett.* **B166** (1986) 196.

[2] http://hallaweb.jlab.org/parity/prex/.

[3] M. Pospelov, *Secluded U(1) below the weak scale*, 0811.1030.

[4] **BABAR** Collaboration, B. Aubert *et al.*, *Search for Dimuon Decays of a Light Scalar in Radiative Transitions Y(3S) -¿ gamma A0*, 0902.2176.

[5] J. D. Bjorken *et al.*, *Search for Neutral Metastable Penetrating Particles Produced in the SLAC Beam Dump*, *Phys. Rev.* **D38** (1988) 3375.

[6] E. M. Riordan *et al.*, *A Search for Short Lived Axions in an Electron Beam Dump Experiment*, *Phys. Rev. Lett.* **59** (1987) 755.

[7] A. Bross *et al.*, *A Search for Shortlived Particles Produced in an Electron Beam Dump*, *Phys. Rev. Lett.* **67** (1991) 2942–2945.

[8] J. D. Bjorken, R. Essig, P. Schuster, and N. Toro, *New Fixed-Target Experiments to Search for Dark Gauge Forces*, *Phys. Rev.* **D80** (2009) 075018, [0906.0580].

[9] K. R. Dienes, C. F. Kolda, and J. March-Russell, *Kinetic mixing and the supersymmetric gauge hierarchy*, *Nucl. Phys.* **B492** (1997) 104–118, [hep-ph/9610479].

[10] S. A. Abel and B. W. Schofield, *Brane-antibrane kinetic mixing, millicharged particles and SUSY breaking*, *Nucl. Phys.* **B685** (2004) 150–170, [hep-th/0311051].

[11] M. J. Strassler and K. M. Zurek, *Echoes of a hidden valley at hadron colliders*, *Phys. Lett.* **B651** (2007) 374–379, [hep-ph/0604261].

[12] S. A. Abel, M. D. Goodsell, J. Jaeckel, V. V. Khoze, and A. Ringwald, *Kinetic Mixing of the Photon with Hidden U(1)s in String Phenomenology*, *JHEP* **07** (2008) 124, [0803.1449].

[13] A. Ringwald, *From Axions to Other WISPs*, 0810.3106.

[14] M. Baumgart, C. Cheung, J. T. Ruderman, L.-T. Wang, and I. Yavin, *Non-Abelian Dark Sectors and Their Collider Signatures*, *JHEP* **04** (2009) 014, [0901.0283].

[15] N. Arkani-Hamed and N. Weiner, *LHC Signals for a SuperUnified Theory of Dark Matter*, *JHEP* **12** (2008) 104, [0810.0714].

[16] C. Cheung, J. T. Ruderman, L.-T. Wang, and I. Yavin, *Kinetic Mixing as the Origin of Light Dark Scales*, 0902.3246.

[17] D. E. Morrissey, D. Poland, and K. M. Zurek, *Abelian Hidden Sectors at a GeV*, 0904.2567.

[18] A. Katz and R. Sundrum, *Breaking the Dark Force*, 0902.3271.

[19] R. Essig, P. Schuster, and N. Toro, *Probing Dark Forces and Light Hidden Sectors at Low-Energy e+e- Colliders*, 0903.3941.

[20] **PAMELA** Collaboration, O. Adriani *et al.*, *Observation of an anomalous positron abundance in the cosmic radiation*, 0810.4995.

[21] **The Fermi LAT** Collaboration, A. A. Abdo *et al.*, *Measurement of the Cosmic Ray e+ plus e- spectrum from 20 GeV to 1 TeV with the Fermi Large Area Telescope*, 0905.0025.

[22] J. Chang *et al.*, *An excess of cosmic ray electrons at energies of 300.800 GeV*, *Nature* **456** (2008) 362–365.

[23] **H.E.S.S.** Collaboration, F. Aharonian *et al.*, *The energy spectrum of cosmic-ray electrons at TeV energies*, *Phys. Rev. Lett.* **101** (2008) 261104, [0811.3894].

[24] **H.E.S.S.** Collaboration, F. Aharonian, *Probing the ATIC peak in the cosmic-ray electron spectrum with H.E.S.S*, 0905.0105.

[25] D. P. Finkbeiner, *Microwave ISM Emission Observed by WMAP*, *Astrophys. J.* **614** (2004) 186–193, [astro-ph/0311547].

[26] G. Dobler, D. P. Finkbeiner, I. Cholis, T. R. Slatyer, and N. Weiner, *The Fermi Haze: A Gamma-Ray Counterpart to the Microwave Haze*, 0910.4583.

[27] N. Arkani-Hamed, D. P. Finkbeiner, T. R. Slatyer, and N. Weiner, *A Theory of Dark Matter*, *Phys. Rev.* **D79** (2009) 015014, [0810.0713].

[28] M. Pospelov and A. Ritz, *Astrophysical Signatures of Secluded Dark Matter*, *Phys. Lett.* **B671** (2009) 391–397, [0810.1502].

[29] J. Hisano, S. Matsumoto, and M. M. Nojiri, *Explosive dark matter annihilation*, *Phys. Rev. Lett.* **92** (2004) 031303, [hep-ph/0307216].

[30] J. March-Russell, S. M. West, D. Cumberbatch, and D. Hooper, *Heavy Dark Matter Through the Higgs Portal*, *JHEP* **07** (2008) 058, [0801.3440].

[31] M. Cirelli, M. Kadastik, M. Raidal, and A. Strumia, *Model-independent implications of the e+, e-, anti-proton cosmic ray spectra on properties of Dark Matter*, *Nucl. Phys.* **B813** (2009) 1–21, [0809.2409].

[32] I. Cholis, G. Dobler, D. P. Finkbeiner, L. Goodenough, and N. Weiner, *The Case for a 700+ GeV WIMP: Cosmic Ray Spectra from ATIC and PAMELA*, 0811.3641.

[33] I. Cholis, D. P. Finkbeiner, L. Goodenough, and N. Weiner, *The PAMELA Positron Excess from Annihilations into a Light Boson*, 0810.5344.

[34] Y. Cui, D. E. Morrissey, D. Poland, and L. Randall, *Candidates for Inelastic Dark Matter*, *JHEP* **05** (2009) 076, [0901.0557].

[35] A. Sommerfeld *Ann. Phys.* **11** (1931) 257.

[36] O. Adriani *et al.*, *A new measurement of the antiproton-to-proton flux ratio up to 100 gev in the cosmic radiation*, 0810.4994.

[37] D. Alves, S. R. Behbahani, P. Schuster, and J. G. Wacker, *Composite Inelastic Dark Matter*, 0903.3945.

[38] D. Tucker-Smith and N. Weiner, *Inelastic dark matter*, *Phys. Rev.* **D64** (2001) 043502, [hep-ph/0101138].

[39] S. Chang, G. D. Kribs, D. Tucker-Smith, and N. Weiner, *Inelastic Dark Matter in Light of DAMA/LIBRA*, 0807.2250.

[40] R. Bernabei *et al.*, *Dark matter particles in the galactic halo: Results and implications from DAMA/NaI*, *Int. J. Mod. Phys.* **D13** (2004) 2127–2160, [astro-ph/0501412].

[41] **DAMA** Collaboration, R. Bernabei *et al.*, *First results from DAMA/LIBRA and the combined results with DAMA/NaI*, *Eur. Phys. J.* **C56** (2008) 333–355, [0804.2741].

[42] A. W. Strong *et al.*, *Gamma-ray continuum emission from the inner Galactic region as observed with INTEGRAL/SPI*, *Astron. Astrophys.* **444** (2005) 495, [astro-ph/0509290].

[43] D. P. Finkbeiner and N. Weiner, *Exciting Dark Matter and the INTEGRAL/SPI 511 keV signal*, *Phys. Rev.* **D76** (2007) 083519, [astro-ph/0702587].

[44] **Muon G-2** Collaboration, G. W. Bennett *et al.*, *Final report of the muon E821 anomalous magnetic moment measurement at BNL*, *Phys. Rev.* **D73** (2006) 072003, [hep-ex/0602035].

[45] **HyperCP** Collaboration, H. Park *et al.*, *Evidence for the decay Sigma+ → p mu+ mu-*, *Phys. Rev. Lett.* **94** (2005) 021801, [hep-ex/0501014].

[46] **The BABAR** Collaboration, B. Aubert, *Search for Dimuon Decays of a Light Scalar in Radiative Transitions Y(3S) → γA0*, 0902.2176.

[47] M. Reece and L.-T. Wang, *Searching for the light dark gauge boson in GeV-scale experiments*, 0904.1743.

[48] **KTeV** Collaboration, E. Abouzaid *et al.*, *Measurement of the rare decay pi0 → e+ e-*, *Phys. Rev.* **D75** (2007) 012004, [hep-ex/0610072].

[49] Bossi, F., private communication.

[50] K. J. Kim and Y.-S. Tsai, *Improved Weizsäcker-Williams methos and its application to lepton and W-boson pair productions*, *Phys. Rev.* **D8** (1973) 3109.

[51] Y.-S. Tsai, *Pair Production and Bremsstrahlung of Charged Leptons*, *Rev. Mod. Phys.* **46** (1974) 815.

[52] Y.-S. Tsai, *Axion Bremsstrahlung by and electron beam*, *Phys. Rev.* **D34** (1986) 1326.

[53] **Particle Data Group** Collaboration, C. Amsler *et al.*, *Review of particle physics*, *Phys. Lett.* **B667** (2008) 1.

[54] *NIM A522* **A522** (2004) 294–346.

[55] J. Alwall *et al.*, *MadGraph/MadEvent v4: The New Web Generation*, *JHEP* **09** (2007) 028, [0706.2334].

[56] D. Wiser *Ph.D. thesis, University of Wisconsin* (1977).

[57] V. Budnev *et al. Phys. Rep.* **15C** (1975) 181.

[58] J. O'Connell and J. Lightbody, *Computer codes QFS and EPC*, *Comp. in Phys.* **May-June 57** (1998).

[59] E04-012 (http://hallaweb.jlab.org/experiment/E04-012/), Y. Qiang, private communication.

[60] H. Burfeindt *et al. Physics Letters* **43B** (1973) 345.

[61] H. Burfeindt *et al. Nucl. Phys.* **B74** (1974) 189.

[62] A. Boyarsli *et al. PRD* **14** (1976) 1733.

[63] P. Degtyarenko, M. Kossov, and H.-P. Wellisch, *Chiral Invariant Phase Space Event Generator, I. Nucleon-antinucleon annihilation at rest*, *Eur. Phys. J. A* **8** (2000) 217.

[64] Y. S. Tsai and V. Whitis, *Thick-target bremsstrahlung and target considerations for secondary-particle production by electrons*, *Phys. Rev.* **149** (Sep, 1966) 1248–1257.

[65] P. Perez and A. Rosowsky *NIM* **A532** (2004) 523.

[66] J. J. LeRose *et al. Nucl.Phys.* **A804** (2008) 116–124.

[67] I. Rachek *et al. Hall A annual report* (2007) 13–15.